

255800-15-F (Vol. I)

**SAR Imaging via Modern 2-D Spectral Estimation Methods**  
*Volume I, Imaging Methods Final Report*

Dr. S. R. DeGraaf

May 1995

DISTRIBUTION STATEMENT A

Approved for public release;  
Distribution Unlimited

Prepared for:  
Advanced Research Projects Agency  
3701 North Fairfax Drive  
Arlington, VA 22203-1714

Contract Number DAAH01-93-C-R178  
ARPA Order No. A284



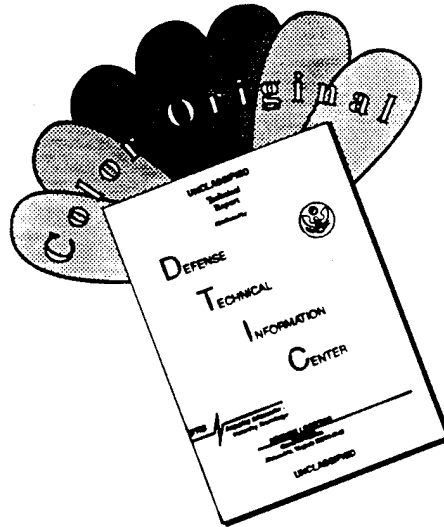
**ERIM**

P.O. Box 134001  
Ann Arbor, MI 48113-4001

19960201 054

DTIC QUALITY INSPECTED 8

# DISCLAIMER NOTICE



THIS DOCUMENT IS BEST QUALITY AVAILABLE. THE COPY FURNISHED TO DTIC CONTAINED A SIGNIFICANT NUMBER OF COLOR PAGES WHICH DO NOT REPRODUCE LEGIBLY ON BLACK AND WHITE MICROFICHE.

ERIM-320		<b>REPORT DOCUMENTATION PAGE</b>		Form Approved OMB No. 0704-0188	
Public reporting burden for the collection of information is estimated to average 1 hour per response, including the time for reviewing instructions, searching existing data sources, gathering and maintaining the data needed, and completing and reviewing the collection of information. Send comments regarding this burden estimate or any other aspect of this collection of information, including suggestions for reducing this burden, to Washington Headquarters Services, Directorate for Information Operations and Reports, 1215 Jefferson Davis Highway, Suite 1204, Arlington, VA 22202-4302, and to the Office of Management and Budget, Paperwork Reduction Project (0704-0188), Washington, DC 20503.					
1. AGENCY USE ONLY (Leave Blank)		2. REPORT DATE May 1995		3. REPORT TYPE AND DATES COVERED Final Scientific & Technical Report, 9/93-10/94	
4. TITLE AND SUBTITLE SAR Imaging via Modern 2-D Spectral Estimation Methods Volume I, Imaging Methods Final Report				5. FUNDING NUMBERS Phase 1: \$184,136 Phase 2: \$185,267 Total: \$369,403	
6. AUTHOR(S) Dr. S. R. DeGraaf					
7. PERFORMING ORGANIZATION NAME(S) AND ADDRESS(ES) Environmental Research Institute of Michigan P. O. Box 134001 Ann Arbor, MI 48113-4001				8. PERFORMING ORGANIZATION REPORT NUMBER 255800-15-F (Vol. I)	
9. SPONSORING/MONITORING AGENCY NAME(S) AND ADDRESS(ES) Advanced Research Projects Agency 3701 North Fairfax Drive Arlington, VA 22203-1714				10. SPONSORING/MONITORING AGENCY REPORT NUMBER	
11. SUPPLEMENTARY NOTES					
12a. DISTRIBUTION/AVAILABILITY STATEMENT				12b. DISTRIBUTION CODE	
13. ABSTRACT (Maximum 200 words) This report discusses the use of modern 2-D spectral estimation algorithms for SAR imaging, and makes two principal contributions to the field of adaptive SAR imaging. First, it is a comprehensive comparison of 2-D spectral estimation methods for SAR imaging. It provides a synopsis of the algorithms available, discusses their relative merits for SAR imaging, and illustrates their performance on simulated and collected SAR imagery. The discussion of autoregressive linear predictive techniques (ARLP), including the Tufts-Kumaresan variant, is somewhat more general than appears in most of the literature, in that it allows the prediction element to be varied throughout the subaperture. This generality leads to a theoretical link between ARLP and one of Pisarenko's methods. The report also provides a theoretical analysis that predicts the impact of the adaptive sidelobe reduction (ASR) algorithm on target-to-clutter ratio and provides insight into order and constraint selection. Second, this work develops multi-channel variants of three related algorithms, minimum variance method (MVM), reduced-rank MVM (RRMVM), and ASR to estimate both reflectivity intensity and interferometric height from polarimetric displaced-aperture interferometric data. Examples illustrate that MVM and ASR both offer significant advantages over Fourier methods for estimating both scattering intensity and interferometric height, and allow empirical comparison of the accuracies of Fourier, MVM, and ASR interferometric height estimates.					
14. SUBJECT TERMS multi-channel SAR imaging, 2-D spectral estimation, superresolution, speckle reduction, interferometry				15. NUMBER OF PAGES 50	
				16. PRICE CODE	
17. SECURITY CLASSIFICATION OF REPORT UNCLASSIFIED	18. SECURITY CLASSIFICATION OF THIS PAGE UNCLASSIFIED	19. SECURITY CLASSIFICATION OF ABSTRACT UNCLASSIFIED	20. LIMITATION OF ABSTRACT		

# CONTENTS

FIGURES .....	iv
ABSTRACT .....	1
1. INTRODUCTION .....	1
2. 2-D SPECTRAL ESTIMATION ALGORITHMS .....	2
2.1 Synopsis of Algorithms .....	2
2.1.1 Fourier Transform .....	7
2.1.2 Periodogram .....	7
2.1.3 MVM .....	7
2.1.4 RRMVM.....	8
2.1.5 ASR.....	10
2.1.6 SVA .....	17
2.1.7 Auto-Regressive Linear Prediction.....	17
2.1.8 ARLP Spectral Averaging and Pisarenko's Method.....	18
2.1.9 Signal-Noise Subspace Decomposition.....	19
2.1.10 Eigenvector and MUSIC .....	20
2.1.11 Tufts-Kumaresan ARLP .....	21
2.1.12 Parametric Maximum Likelihood.....	22
2.2 Simulated Point-Scattering Results .....	23
2.3 Collected Scalar SAR Results .....	24
3. Interferometric and Polarimetric MVM, RRMVM, and ASR .....	27
3.1 DCS IFSAR Examples .....	29
4. Conclusions .....	33
5. Acknowledgements .....	34
References .....	35

## FIGURES

1. Extraction of a single signal history subaperture from within the full (decimated) aperture. ....	38
2. Decimation of signal history to represent a sub-image region of interest. ....	38
3. Comparison of theoretically predicted and observed TCR gain provided by the ASR algorithm as a function of input TCR for nonseparable and separable filters using constraints satisfying. ....	38
4. Comparison of 2-D spectral estimation techniques for imaging synthetic point scatterers. Image-domain TCR is 33dB. ....	39
5. Comparison of 2-D spectral estimation techniques for imaging synthetic point scatterers. Image-domain TCR is 13dB. ....	40
6. Baseline Taylor-weighted (-35dB, N=5) Fourier imagery. ....	41
7. 40% subaperture MVM imagery. ....	41
8. 400/402 subaperture RRMVM (c=1.0002) imagery. ....	42
9. ASR (order=2, c=.5) imagery. ....	42
10. SVA imagery. ....	43
11. Unweighted (sinc IPR) Fourier imagery. ....	43
12. 40% subaperture ARLP (first- and second-quad. avg.) imagery. ....	44
13. 40% subaperture Pisarenko imagery. ....	44
14. 40% subaperture EV imagery (90% energy order criterion). ....	45
15. Interpolated slices through trihedral on causeway, "easy" methods. ....	45
16. Interpolated slices through trihedral on causeway, "hard" methods. ....	45
17. Geometric and conceptual foundation of interferometric SAR imaging. ....	46
18. Baseline Taylor-weighted (-35dB, n=5) Fourier interferogram. ....	47
19. 40% subaperture MVM interferogram. ....	48
20. SVA interferogram. ....	49
21. ASR (order 4, c=.25) interferogram. ....	50

## Abstract

This paper discusses the use of modern 2-D spectral estimation algorithms for SAR imaging, and makes two principal contributions to the field of adaptive SAR imaging. First, it is a comprehensive comparison of 2-D spectral estimation methods for SAR imaging. It provides a synopsis of the algorithms available, discusses their relative merits for SAR imaging, and illustrates their performance on simulated and collected SAR imagery. The discussion of autoregressive linear predictive techniques (ARLP), including the Tufts-Kumaresan variant, is somewhat more general than appears in most of the literature, in that it allows the prediction element to be varied throughout the subaperture. This generality leads to a theoretical link between ARLP and one of Pisarenko's methods. The paper also provides a theoretical analysis that predicts the impact of adaptive sidelobe reduction (ASR) algorithm on target-to-clutter ratio and provides insight into order and constraint selection. Second, this work develops multi-channel variants of three related algorithms, minimum variance method (MVM), reduced-rank MVM (RRMVM), and ASR to estimate both reflectivity intensity and interferometric height from polarimetric displaced-aperture interferometric data. Examples illustrate that MVM and ASR both offer significant advantages over Fourier methods for estimating both scattering intensity and interferometric height, and allow empirical comparison of the accuracies of Fourier, MVM, and ASR interferometric height estimates.

## 1 Introduction

Synthetic aperture radar (SAR) imaging can be viewed as a parameter estimation problem in which one seeks to estimate the scene reflectivity intensity vs. slant-plane location, i.e. an intensity image. Interferometric SAR systems also seek to estimate scattering height out of the slant-plane, which is proportional to the phase difference, pixel-by-pixel, between registered images formed from a pair of coherent, vertically displaced measurement apertures. Here we discuss the limitations of conventional Fourier methods for estimating intensity and interferometric height images, and the rationale for employing alternative 2-D spectral estimation methods. Section 2 provides a synopsis of 2-D spectral estimation algorithms, discusses their relative merits for SAR imaging, and compares scalar imagery produced by these algorithms for both synthetic point scattering data and data collected of two commercial ships near Toledo, OH. This section also develops a theoretical model for the impact of adaptive sidelobe reduction (ASR) filter order and constraint on target-to-clutter ratio that sheds light on strategies for selecting these parameters. Section 3 generalizes three algorithms that hold promise for polarimetric and interferometric application, and uses data collected of the area around the University of Michigan football stadium to illustrate that the minimum variance method (MVM) and adaptive sidelobe reduction (ASR) algorithm both offer significant advantages over Fourier methods for interferometric SAR imaging. This section also provides an empirical comparison of the accuracies of Fourier, MVM, and ASR interferometric height estimates. Section 4 summarizes and draws conclusions. All SAR data shown was collected by the Wright Laboratory-ERIM Data Collection System (DCS) SAR, which is installed on a CV-580 aircraft, and operates at a variety of frequency bands, resolutions, and polarizations, in spotlight and stripmap modes. The DCS supports research in multichannel SAR, where the channels can represent multiple frequencies, multiple polarizations, and/or multiple interferometric apertures.

Fourier SAR imaging exploits the Fourier transform pair relationship between signal history measurements (polar-to-rectangular [1] or migration [2] formatted) and scene reflectivity. Fourier imaging exhibits several drawbacks for imaging interferometric intensity and phase/height. First, as the collection apertures are of finite size in  $k$ -space, the

spatial resolution afforded by Fourier imaging is inherently limited. Typically, Taylor or Kaiser-Bessel weightings are employed to control impulse response (IPR) peak sidelobe and integrated sidelobe level. The artifacts (poor resolution and sidelobe artifacts) induced in Fourier SAR imagery by a fixed system IPR are often undesirable. Second, finite resolution leads to the classical coherent imaging speckle phenomenon, which is caused by scintillation of independent unresolved scattering elements. Complex circular white Gaussian noise, with standard deviation (RMS level)  $\sigma$ , is a common signal history domain model for the scattering from a patch of homogeneous clutter. The corresponding unweighted Fourier transform image is also complex circular white Gaussian noise. The magnitude of this Fourier image is Rayleigh distributed, with mean and standard deviation that are both proportional to  $\sigma$ . The classic description of SAR image speckle as “multiplicative noise” stems from the fact that the Fourier transform is not an appropriate estimator for  $\sigma$ . On the other hand, a power spectral density (PSD) estimator is appropriate for estimating  $\sigma$ . PSD estimators are also appropriate for estimating the scattering intensity of deterministic scatterers. Third, thermal noise, horizontally unresolved scatterers, and IPR integrated sidelobe level all contribute to interferometric phase noise which degrades the accuracy of interferometric height estimates. Generally, height accuracy improves with increasing SNR. Often, some form of smoothing or filtering is necessary to reduce the phase/height noise associated clutter and target scattering.

Modern spectral estimation techniques offer attractive alternatives to Fourier SAR imaging. These non-linear techniques offer the promise of improved resolution and contrast, and reduced speckle. Improvements in resolution and reductions in sidelobe artifacts arise through adaptive interference nulling, linear predictive modeling, signal-noise subspace decomposition, or parametric sinusoidal signal history (point scatterer) modeling. Speckle reduction arises through the signal history domain averaging implicit in PSD image estimation. Contrast improvement arises through signal-noise subspace decomposition or algorithm singularities. Similarly, interferometric variants of some of these algorithms offer the promise of reduced phase/height noise and improved phase/height accuracy through enhanced resolution and averaging.

## 2 2-D Spectral Estimation Algorithms

In this section, we summarize the available 2-D spectral estimation algorithms, review the theory behind them, and discuss their relative advantages for SAR imaging. In addition, we illustrate their performance on both simulated and collected SAR data.

### 2.1 Synopsis of Algorithms

Table 1 summarizes the rationale and formulation of a variety of 2-D spectral estimation algorithms. The table groups the algorithms on the basis of their rationale. Many of these algorithms are discussed in [3-6], and in a vast spectral estimation and array processing literature, for example [7-31]. However, RRMVM [43], ASR [44,45]

and SVA [47] are new, as is much of the literature describing the application of spectral estimation algorithms to radar RCS analysis and imaging [32-47]. Moving from the top of the table toward the bottom, the degree to which the algorithms exploit a point scattering (sinusoidal signal history) model increases. As the algorithms exploit this model to a higher degree, their resolution and accuracy improves, provided the model is valid. However, the high performance algorithms are less robust when the model is compromised. While Fourier SAR imagery is often characterized by “prominent points,” the sinusoidal signal history model can be compromised in the cross-range dimension by a variety of common physical phenomena: glints, sliding speculars, creeping waves, resonances and motion-induced phase errors. Similarly, frequency-dependent scattering amplitude, characteristic of certain types of scattering, can compromise the sinusoidal model in the range dimension for systems that exploit a large fractional bandwidth.

Technique	Rationale	PSD or Coherent Spectrum
FFT	non-adaptive filterbank	$\underline{W}^H(r) \underline{A} \underline{X}$
ASR	adaptive filterbank	adaptively FIR filter $\underline{W}^H(r) \underline{X}$
SVA	special case of ASR	adaptively FIR filter $\underline{W}^H(r) \underline{X}$
periodogram	non-adaptive filterbank expected output energy	$\underline{W}^H(r) \underline{A} \underline{R} \underline{A} \underline{W}(r)$
RRMVM	reduced-rank MVM	$\frac{\underline{W}^H(r) (\underline{\mu}(r) \underline{I} + \underline{R})^{-1} \underline{R} (\underline{\mu}(r) \underline{I} + \underline{R})^{-1} \underline{W}(r)}{(\underline{W}^H(r) (\underline{\mu}(r) \underline{I} + \underline{R})^{-1} \underline{W}(r))^2}$
MVM	adaptive filterbank expected output energy	$\frac{1}{\underline{W}^H(r) \underline{R}^{-1} \underline{W}(r)}$
ARLP	linear data extrapolation AR system driven by white noise	$\sqrt{R_{P,P}^{-1}}; \text{ also } \underline{A}_P = -\underline{R}_P^{-1} \underline{r}_P^*$ and $\frac{1}{\sqrt{R_{P,P}^{-1}}  \underline{A}_P^H \underline{W}(r) }$
Pisarenko	RMS average over pred. elem. of reciprocal ARLP spectra	$\frac{1}{\sqrt{\underline{W}^H(r) \underline{R}^{-2} \underline{W}(r)}}$
EV/MUSIC	signal-noise subspace decomposition within MVM framework	$\frac{1}{\underline{W}^H(r) (\sum_{\text{noise}} \lambda_m^{-1} \underline{V}_m \underline{V}_m^H) \underline{W}(r)}$ or $\frac{1}{\underline{W}^H(r) (\sum_{\text{noise}} \sigma_o^{-2} \underline{V}_m \underline{V}_m^H) \underline{W}(r)}$
TKARLP	signal-noise subspace decomposition within ARLP framework	$\underline{A}_P = -\underline{R}_{P, sig}^\dagger \underline{r}_P^*$ and $\frac{1}{ \underline{A}_P^H \underline{W}(r) }$
PML	max-likelihood estimates of complex amplitudes and frequencies of sinusoids in AWGN	parametric: nonlinear least-squares and regression

Table 1: Synopsis of 2-D spectral estimation algorithm rationale and formulation.

The mathematical notation in Table 1 is as follows. The elements of vector  $\underline{X}$  are the rectangularly formatted 2-D radar signal history samples. The elements of vector  $\underline{W}(r)$  are the exponential coefficients of a 2-D Fourier transform tuned to spatial location  $r$ . If the 2-D data is raster-scanned into the vector  $\underline{X}$ , then  $\underline{W}(r)$  can be described as a Kronecker product of 1-D Fourier transform vectors. Diagonal matrix  $\underline{A}$  represents a real-valued signal history weighting function used to control the tradeoff between Fourier IPR mainlobe and sidelobes. Signal



history correlation matrix  $\mathbf{R}$  represents an estimate of the expected matrix  $E(\mathbf{X}\mathbf{X}^H)$ .  $\{\lambda_m\}$  and  $\{\mathbf{V}_m\}$  represent the eigenvalues and orthonormal eigenvectors, respectively, of  $\mathbf{R}$ . Superscript  $H$  denotes conjugate transpose. Prediction indicator vector  $\underline{P}$  has a one in the  $P^{th}$  element, corresponding to the signal history element being predicted, and zeros elsewhere. Matrix  $\mathcal{R}_P$  omits the  $P^{th}$  row and column of signal history correlation matrix  $\mathbf{R}$ , while vector  $\underline{r}_P$  represents the correlations between the data point being predicted and the data samples used to predict it, i.e. the column of  $\mathbf{R}$  that is missing in  $\mathcal{R}_P$ .  $\mathcal{R}_{P, sig}^\dagger$  is the pseudo inverse of the signal contribution to  $\mathcal{R}_P$ , which is evaluated via SVD or eigen decomposition.

The Fourier transform (FFT) and adaptive sidelobe reduction (ASR) algorithm both produce coherent (complex-valued) spectra. These coherent images represent the outputs of banks of 2-D narrowband filters, where each filter output is tuned to a given spatial location. The FFT represents a bank of fixed narrowband filters, while the ASR algorithm represents a bank of adaptive narrowband filters. The FFT image is a convolution between the scene reflectivity and a space-invariant impulse response. In contrast, the ASR image is a convolution between the scene reflectivity and a space-variant impulse response. One computes the ASR image by applying a space-variant FIR filter to a uniformly weighted (sinc IPR) Fourier image, and chooses the ASR filter coefficients to maximize the output signal-to-interference-ratio (SIR) in a single-realization sense. Signal is defined to be the complex sinusoid in the signal history domain that corresponds to a point scatterer at the tuned spatial location, while interference consists of interfering tones, i.e. point scatterers at other locations, together with clutter and noise. Both separable and nonseparable 2-D implementations are possible; for a given order, the nonseparable filter provides more adaptive degrees of freedom. Space variant apodization (SVA) [47] is a special case of ASR that employs a single degree of freedom, together with a constraint motivated by the oscillatory nature of the sidelobes of a sinc IPR.

The periodogram, minimum variance method (MVM), and reduced-rank MVM (RRMVM) all produce power spectral density (positive semi-definite, real-valued) spectra. These PSD images represent the average, or expected value, of the output energies of a bank of 2-D narrowband filters, where each filter output is tuned to a given spatial location. The periodogram represents a bank of fixed narrowband filters, while MVM and RRMVM represent adaptive narrowband filters. In each case, a correlation matrix  $\mathbf{R}$ , whose entries are an estimate of the correlations between signal history domain data samples, must be estimated from the signal history data. For the periodogram, the correlation matrix can be singular, i.e. of less than full rank. Both MVM and RRMVM compute narrowband filters that maximize the output SIR in an expected or average sense. MVM requires a full-rank, nonsingular correlation matrix estimate, which implies a large amount of averaging, while RRMVM accommodates a reduced-rank, singular correlation matrix based on a small amount of averaging.

Both ASR and RRMVM share the spirit of MVM in that they seek to maximize SIR. However, both are “singular” methods in that they optimize SIR on the basis of low-rank (unit-rank for ASR) signal history correlation matrices. Because of this singularity, constraints must be imposed to insure non-zero output. Both algorithms employ a

constraint on the  $l_2$  norm of a weighting vector. Choice of the constraint value controls the behavior of the algorithms. For reasonable choices of filter order (ASR) or degree of averaging (RRMVM), these algorithms enjoy a considerable computational advantage over the other adaptive methods.

Autoregressive linear prediction (ARLP) methods predict signal history samples as linear combinations of the neighboring signal history samples, and select the predictor filter coefficients to minimize average prediction error. Theoretically, based on the assumption that the prediction error signal is an innovations process, i.e. white noise, the PSD estimate equals the minimized prediction error energy divided by the magnitude squared of the transfer function. However, it is known that the PSD should be chosen as the square root of this quantity to obtain correct scaling [6,12]. The signal history sample being predicted need not have any particular ordinal relation to the samples being used to predict it. In other words, the filter need not be causal, semi-causal, etc. ARLP imagery based on any one choice of prediction element may exhibit spiky behavior and elliptical, rather than circular, contours. While our experience does not suggest any reason to prefer one choice over another, we have found it desirable to use an average image based on several prediction elements. In particular, we have found it useful to evaluate an RMS average ARLP image, whose inverse is the RMS average of the inverse ARLP images yielded by all possible prediction elements. If one makes the generally invalid assumption that the individual ARLP filters yield the same prediction error energy, then the RMS ARLP image reduces to one of Pisarenko's spectral estimates. Nevertheless, in practice, the differences between RMS ARLP imagery and Pisarenko imagery are negligible. Our experience with real SAR data suggests that, that Pisarenko imagery is somewhat sharper than MVM imagery, but exhibits greater background clutter variability and lower contrast. However, as one might anticipate from the similarity in their functional form, Pisarenko and MVM imagery is fairly similar.

Eigenvector (EV) and Multiple Signal Classification (MUSIC) methods can be viewed as variants of the MVM spectrum that cause the image peaks corresponding to high-TCR point scatterers to become very sharp and high (tending toward infinity). Indeed, the rationale for these methods is that the orthonormal eigenvectors of  $\mathbf{R}$  that span the noise subspace are orthogonal to the signal vectors corresponding to prominent point scatterers. The height of these peaks is a measure of "pointiness" rather than of scattering intensity. EV and MUSIC methods differ in that MUSIC explicitly whitens, or equalizes, the noise eigenvalues, while EV does not. In our experience, this whitening destroys the spatial inhomogeneities associated with terrain clutter or other diffuse scattering in SAR imagery; thus MUSIC is not generally suitable for SAR imaging. In contrast, the EV method preserves the clutter inhomogeneities, while smoothing speckle, and enhancing the sharpness and contrast of prominent point scatterers.

Tufts-Kumaresan ARLP (TKARLP) methods are based on a signal-noise subspace decomposition in the framework of ARLP. In this case, the noise contribution to the correlation matrix is omitted to boost the apparent SNR. Further, the TKARLP prediction filter is chosen on the basis of the pseudo-inverse of the signal portion of a singular correlation matrix, which allows larger subaperture sizes to be used, thereby improving resolution. As with

conventional ARLP, we find that TKARLP imagery based on any one choice of prediction element may exhibit spiky behavior and elliptical, rather than circular, contours. Again, our experience does not suggest any reason to prefer one choice over another, but we have found it desirable to employ an inverse RMS average TKARLP image based on first- and second-quadrant predictors.

A variety of methods can be employed to estimate the correlation matrix from the signal history data: subaperture averaging (covariance method), forward-backward subaperture averaging (modified covariance method), block-Toeplitz enforcement (biased or unbiased correlation method), and decimation averaging. These averaging schemes need not be viewed as distinct alternatives; rather, they can be combined. In the literature, certain combinations of algorithm class and averaging schemes tend to be referred to as specific algorithms, which obscures the fact that any algorithm class can be combined with any averaging scheme. Both biased and unbiased correlation methods yield poor results in a variety of spectral estimation applications, including SAR imaging. The sole virtue of the correlation method is the reduction in computational complexity afforded by block-Toeplitz correlation structure. In our work, we prefer, and use, forward-backward subaperture averaging, in conjunction with all 2-D spectral estimation algorithms that utilize a correlation matrix.

Figure 1 illustrates how subaperture averaging works. For uni-directional (forward) averaging, the correlation matrix estimate is an average of  $A = (K_x - \hat{K}_x + 1)(K_y - \hat{K}_y + 1)$  outer-products which represent all possible subapertures within the full aperture:

$$\mathbf{R}_{UD} = \frac{1}{A} \sum_{i,j} \underline{X}_{i,j} \underline{X}_{i,j}^H. \quad (1)$$

For forward-backward averaging, the correlation matrix estimate is an average of  $2A$  outer-products,

$$\mathbf{R}_{FB} = \frac{1}{2A} \sum_{i,j} \underline{X}_{i,j} \underline{X}_{i,j}^H + \frac{1}{2A} \sum_{i,j} \mathbf{J} \underline{X}_{i,j}^* \underline{X}_{i,j}^T \mathbf{J} = \frac{1}{2} (\mathbf{R}_{UD} + \mathbf{J} \mathbf{R}_{UD}^T \mathbf{J}), \quad (2)$$

which exploits the fact that a 2-D sinusoid evolves in one spatial direction in the same manner as the conjugate sinusoid evolves in the opposite spatial direction, while conjugating and reversing the noise contribution effectively yields an independent noise realization. To obtain a non-singular correlation matrix, we require  $A \geq \hat{K}_x \hat{K}_y$  for unidirectional averaging, and  $2A \geq \hat{K}_x \hat{K}_y$  for forward-backward averaging. Forward-backward averaging effectively doubles the amount of averaging that occurs.

In practice, all of the methods that require evaluation, inversion, or eigen decomposition of a full-rank signal history correlation matrix are computationally intensive, on the order of  $(\hat{K}_x \hat{K}_y)^3$ ; for typical amounts of averaging, Tufts-Kumaresan ARLP shares this order of computational complexity. To apply these algorithms to typical SAR scenes in a reasonable timeframe using general purpose workstations, it is necessary to employ a decimation and mosaicing strategy. As shown in Figure 2, the signal history is decimated down by factors  $D_x$  and  $D_y$  in range

and cross-range dimensions. Decimation is performed so as to obtain the down-sampled SH measurements that correspond to a series of small overlapping subimages within the entire SAR scene. The computational complexity for each subimage drops by a factor of  $(D_x D_y)^3$ . If the  $D_x D_y$  subimages are computed serially, then the overall improvement factor drops to  $(D_x D_y)^2$ . Of course, the individual chips can be computed in parallel.

In those instances where a point scattering model is valid in both range and cross-range dimensions, the parametric maximum likelihood (PML) [17] method provides extremely accurate estimates of both the location of scattering points and their complex scattering amplitudes. This method is not suitable for general SAR imaging, but may be suitable for specialized SAR analysis tasks.

Following is a brief mathematical review of each of the adaptive SAR imaging methods.

### 2.1.1 Fourier Transform

Fourier transform image formation evaluates a linear combination of the signal history samples of the form  $\underline{W}^H(r) \underline{A} \underline{X}$ , where  $\underline{X}$  is a vector of the 2-D signal history samples, and  $\underline{W}(r)$  is a complex-valued sinusoid vector that corresponds to the 2-D signal history measurements that would emanate from a point scatterer at spatial location  $r$ .  $\underline{A}$  is a diagonal matrix whose entries correspond to a separable or nonseparable weighting function used to control the IPR mainlobe/sidelobe tradeoff. Unweighted FFT image formation corresponds to evaluating a bank of matched filter outputs, each filter being matched to a particular spatial location. In the simple case of a single sinusoid in white Gaussian noise, this matched filter maximizes signal-to-interference ratio (SIR). However, in more complicated scenarios, energy from scatterer B can leak through the sidelobes (or even mainlobe) of the IPR tuned to scatterer A, thereby corrupting the estimate of energy scattered from A.

### 2.1.2 Periodogram

The periodogram recognizes the stochastic nature of the data and seeks to estimate the average power output of the Fourier transform, i.e. the power spectral density  $E(|\underline{W}^H(r) \underline{A} \underline{X}|^2) = \underline{W}^H(r) \underline{A} \underline{R} \underline{A} \underline{W}(r)$ . One can view this averaging as the logical extension of "independent look averaging," which is often performed in SAR to reduce image speckle. Of course, subaperture averaging entails a loss of resolution because the subapertures are smaller than the full aperture. For this reason, the periodogram is of little practical interest.

### 2.1.3 MVM

To maximize signal-to-interference ratio (SIR) in each spatial location, Capon's minimum variance method evaluates a different linear combination of the signal history samples, of the form  $\underline{A}^H(r) \underline{X}$ , where the space-variant weighting vector  $\underline{A}(r)$  is complex-valued. Both the amplitude and phase of the components of  $\underline{A}(r)$  can differ from those of the weighted Fourier transform vector  $\underline{A} \underline{W}(r)$ . Thus MVM does more than merely change the real-valued weights in

a Fourier transform. To insure that point scattered energy emanating from location  $\mathbf{r}$  is passed with unit gain, i.e. not attenuated, MVM imposes the constraint  $\underline{A}^H(\mathbf{r})\underline{W}(\mathbf{r}) = 1$ . Since the output consists of desired and undesired energy, and since the desired energy passes with unit gain, MVM maximizes SIR by selecting  $\underline{A}(\mathbf{r})$  to minimize the expected output energy,

$$E(|\underline{A}^H(\mathbf{r})\underline{X}|^2) = \underline{A}^H(\mathbf{r})\mathbf{R}\underline{A}(\mathbf{r}). \quad (3)$$

Solving the constrained optimization via the method of Lagrange multipliers yields

$$\underline{A}(\mathbf{r}) = \frac{\mathbf{R}^{-1}\underline{W}(\mathbf{r})}{\underline{W}^H(\mathbf{r})\mathbf{R}^{-1}\underline{W}(\mathbf{r})} \quad (4)$$

and corresponding optimized output energy, or spectral estimate

$$S_{MVM}(\mathbf{r}) = \frac{1}{\underline{W}^H(\mathbf{r})\mathbf{R}^{-1}\underline{W}(\mathbf{r})}. \quad (5)$$

Evaluating and inverting the correlation matrix  $\mathbf{R}$  dominates the computational complexity of MVM; subsequent evaluation of the quadratic form in equation (5) involves computing a pair of 2-D FFTs.

#### 2.1.4 RRMVM

The reduced-rank minimum variance method also provides a power spectral density estimate that maximizes the expected SIR, where signal is defined as the sinusoidal component of the signal history that arises from point scattering at location  $\mathbf{r}$ . While MVM does this on the basis of a nonsingular, invertible correlation matrix, RRMVM seeks to do this on the basis of a singular, non-invertible correlation matrix. RRMVM circumvents the difficulty of a singular correlation matrix by invoking an additional constraint, namely  $\underline{A}^H(\mathbf{r})\underline{A}(\mathbf{r}) \leq \frac{c^2}{\hat{K}_x\hat{K}_y}$ . The impact of the added constraint is to add a scaled identity matrix to the singular correlation matrix. Thus the optimum RRMVM weight vector is

$$\underline{A}(\mathbf{r}) = \frac{(\mu(\mathbf{r})\mathbf{I} + \mathbf{R})^{-1}\underline{W}(\mathbf{r})}{\underline{W}^H(\mathbf{r})(\mu(\mathbf{r})\mathbf{I} + \mathbf{R})^{-1}\underline{W}(\mathbf{r})}, \quad (6)$$

where the Lagrange multiplier  $\mu(\mathbf{r})$  satisfies

$$\frac{\underline{W}^H(\mathbf{r})(\mu(\mathbf{r})\mathbf{I} + \mathbf{R})^{-1}\underline{W}(\mathbf{r})}{(\underline{W}^H(\mathbf{r})(\mu(\mathbf{r})\mathbf{I} + \mathbf{R})^{-1}\underline{W}(\mathbf{r}))^2} \leq \frac{c^2}{\hat{K}_x\hat{K}_y}. \quad (7)$$

Substituting expression (6) into definition (3) yields the RRMVM PSD image

$$S_{RRMVM}(\mathbf{r}) = \frac{\underline{W}^H(\mathbf{r})(\mu(\mathbf{r})\mathbf{I} + \mathbf{R})^{-1}\mathbf{R}(\mu(\mathbf{r})\mathbf{I} + \mathbf{R})^{-1}\underline{W}^H(\mathbf{r})}{(\underline{W}^H(\mathbf{r})(\mu(\mathbf{r})\mathbf{I} + \mathbf{R})^{-1}\underline{W}(\mathbf{r}))^2}. \quad (8)$$

In the case of full-rank MVM,  $\underline{A}^H(r)\underline{A}(r)$  represents the reciprocal of SNR processing or compression gain against white noise. Thus, one can interpret the new constraint as a means of preventing RRMVM from completely sacrificing white SNR processing gain in its efforts to optimize SIR. In practice, the effect of the new constraint is to prevent the output energy from going to zero in spite of the original unit gain constraint. It is straightforward to show that  $S_{RRMVM}(r) = 0$  for spatial locations where the new constraint is inactive, i.e.  $\mu(r) = 0$ . Use of  $c \leq 1$  allows the algorithm no data adaptation. In conjunction with signal history averaging,  $c \leq 1$  causes RRMVM to reduce to the unweighted periodogram. In the case of a unit-rank correlation matrix (a single full aperture, no averaging), choosing  $c \leq 1$  causes RRMVM to further degenerate to the magnitude-squared of the unweighted Fourier transform. Use of  $c > 1$  allows data adaptation. When averaging is sufficient to insure a full-rank correlation matrix, relaxing the new constraint, i.e. using  $c \rightarrow \infty$ , causes RRMVM to degenerate to MVM.

It is computationally advantageous to evaluate the right singular vectors and values of  $\mathbf{Q} = \mathbf{U}\mathbf{\Sigma}\mathbf{V}^H$ , or equivalently, the eigen decomposition of  $\mathbf{Q}^H\mathbf{Q} = \mathbf{V}\mathbf{\Lambda}\mathbf{V}^H$ , which is dimensionally smaller than  $\text{mat}R = \mathbf{Q}\mathbf{Q}^H$ , where the columns of the data matrix  $\mathbf{Q}$  correspond to the small number of forward-backward data subapertures, and  $\mathbf{\Lambda} = \mathbf{\Sigma}^T\mathbf{\Sigma}$ . Exploiting the matrix inverse lemma, we obtain

$$(\mu\mathbf{I} + \mathbf{R})^{-1} = \frac{1}{\mu}(\mathbf{I} - \mathbf{Q}\mathbf{V}(\mu\mathbf{I} + \mathbf{\Lambda})^{-1}\mathbf{V}^H\mathbf{Q}^H$$

which, when substituted into equations (7) and (8) forms the basis of an efficient computational procedure:

1. evaluate "kernel" correlation matrix  $\mathbf{Q}^H\mathbf{Q}$
2. evaluate eigen decomposition  $\mathbf{Q}^H\mathbf{Q} = \mathbf{V}\mathbf{\Sigma}\mathbf{V}^H$
3. evaluate eigen images, i.e. Fourier transforms of data mapped onto eigenvectors,  $\underline{\omega} = \mathbf{V}^H\mathbf{Q}^H\mathbf{x}$
4. evaluate Lagrange multiplier  $\mu$  by solving  $\frac{\hat{K}_x\hat{K}_y - \sum \frac{2\mu + \lambda_n}{(\mu + \lambda_n)^2} \omega_n^2}{(\hat{K}_x\hat{K}_y - \sum \frac{1}{\mu + \lambda_n} \omega_n^2)^2} \leq \frac{c^2}{\hat{K}_x\hat{K}_y}$
5. evaluate output  $\mu^2 \frac{\sum \frac{\omega_n^2}{(\mu + \lambda_n)^2}}{(\hat{K}_x\hat{K}_y - \sum \frac{\omega_n^2}{\mu + \lambda_n})^2}$

When a small amount of averaging is performed, as is the intent of the algorithm, evaluating the eigen images, step (3), dominates both the computational complexity and storage requirements of RRMVM. The burden of evaluating and storing all of the eigen images makes RRMVM unattractive when a significant amount of averaging is performed. However, our experience suggests that, in very low-rank scenarios, in which either a handful of forward-backward nearly full-aperture subapertures or a handful of forward-backward non-overlapping subapertures are used, the dominant effect of RRMVM is to threshold the corresponding unweighted (sinc IPR) Fourier image. In scenes where the scattering intensity spans a large dynamic range, selecting a constraint  $c$  that is large enough to eliminate the

sidelobe artifacts of prominent scatterers causes weaker scatterers to be eliminated. In conjunction with limited averaging, we have observed significant resolution enhancement by RRMVM only in simple, simulated scenarios. However, in cases where the dynamic range is limited, RRMVM produces cleaner looking intensity imagery than ASR.

As a final note, we have been unable to establish a criterion for selecting reasonable choices of the constraint coefficient  $c$  as a function of the amount of averaging (i.e. correlation matrix rank) that insures consistent RRMVM image characteristics from one SAR scene to the next.

### 2.1.5 ASR

The adaptive sidelobe reduction algorithm extends RRMVM to its logical conclusion, namely maximizing the SIR on the basis of a single, full-aperture realization, or unit-rank correlation matrix. In the process, ASR overcomes the weak signal suppression and computational complexity drawbacks of RRMVM by restricting the number of adaptive degrees of freedom. To do this, ASR imposes a structure on the functional form of the weighting vector. For purposes of clarity, we present the ASR algorithm in a 1-D context, and subsequently discuss its application to multidimensional data. For a single full-aperture we can expand the complex-valued (i.e. omit the magnitude squared) starting point of MVM and RRMVM, namely equation (3), as

$$\hat{x}(r) = \sum_{k=0}^{K-1} A(r, k) X(k) e^{j2\pi \frac{rk}{N}} \quad (9)$$

where we have explicitly broken the complex weighting coefficients into an amplitude term and an exponential Fourier phase factor. Here, we require  $A(r, k)$  to be real-valued; thus, unlike MVM and RRMVM, ASR does not perturb the Fourier transform phase factors. The form of this equation resembles that of a weighted inverse discrete Fourier transform (interpolated by a factor  $R = K/N$ ), with the exception that the weighting coefficients can depend on the spatial tuning location  $r$ . To restrict the number of adaptive degrees of freedom further, ASR requires that the weighting coefficients be of the form

$$A(r, k) = 1 + \sum_{m=1}^M a(r, m) \cos\left(\frac{2\pi mk}{K}\right), \quad (10)$$

where the ASR order  $M$  is small ( $M \ll K$ ). This weighted sum-of- $M$ -cosines form parallels that of a Taylor weighting function of order  $M$ , except that we allow the coefficients to vary with output sample  $r$ . The rationale for this choice is that, for integer interpolation (zero-pad) factors, substituting expression (10) into equation (9) yields

$$\hat{x}(r) = x(r) + \sum_{m=1}^M a(r, m) (x(r - Rm) + x(r + Rm))/2, \quad (11)$$

where  $x(r)$  is the unweighted (sinc IPR) inverse Fourier transform image. Equation (11) says that the ASR image can be evaluated by applying a space-variant, symmetric, non-causal FIR filter to the sinc IPR Fourier image. The unit-gain signal constraint,  $\underline{A}^H(r)\underline{W} = 1$ , is satisfied automatically, regardless of the filter coefficients  $a(r, m)$ . This is clear from the fact that the sinc IPR centered at interpolated sample  $r$  exhibits its zeros at samples  $r \pm mR$ . Thus we maximize the single-realization SIR by selecting the FIR coefficients to minimize  $|\hat{x}(r)|^2$ .

As with RRMVM, in spite of the unit-gain constraint, an additional constraint must be invoked to insure a non-zero ASR image. In this case we impose a constraint on the vector of FIR filter coefficients,  $\underline{a}^T(r)\underline{a}(r) \leq c^2 \leq 1$ . This constraint limits cancellation of the desired spatial frequency sinusoid that can arise from modulating and amplifying the sinusoids from neighboring spatial frequencies via the weighted cosine form of the weighting function.

To formulate the solution for the ASR filter coefficients, it is convenient to treat the complex-valued sinc IPR Fourier image  $x(r)$  and the ASR output image  $\hat{x}(r)$  as real-valued, two-channel (I and Q) vector images,  $\underline{x}(r)$  and  $\underline{\hat{x}}(r)$ , respectively. We also define a real-valued lag matrix  $\underline{L}(r) = (\underline{l}_I(r), \underline{l}_Q(r))$ , where  $\underline{l}_I(r)$  and  $\underline{l}_Q(r)$  are  $M$ -element vectors of the I and Q symmetrically combined channel lags, respectively, around output sample  $r$ . Finally, the ASR filter vector is  $\underline{a}(r) = (a(r, 1), \dots, a(r, M))^T$ . Using this notation, we express (11) as

$$\underline{\hat{x}} = \underline{x} + \underline{L}^T \underline{a}, \quad (12)$$

and suppress the understood dependence on  $r$ . Equation (12) also expresses the operation of a single ASR filter on  $N$ -channel SAR data (such as interferometric, where  $N = 2$ ), if we increase the dimensions of  $\underline{\hat{x}}$  and  $\underline{x}$ , and the number of columns in the lag matrix, to  $2N$ .

We select the ASR filter vector to minimize the output energy (or average multi-channel energy)  $\underline{\hat{x}}^T \underline{\hat{x}}$  subject to  $\underline{a}^T \underline{a} \leq c^2$ . The solution is

$$\underline{a} = -(\mu \underline{I} + \underline{L} \underline{L}^T)^{-1} \underline{L} \underline{x} \quad (13)$$

where the Lagrange multiplier  $\mu$  satisfies the constraint

$$\underline{a}^T \underline{a} = \underline{x}^T \underline{L}^T (\mu \underline{I} + \underline{L} \underline{L}^T)^{-2} \underline{L} \underline{x} \leq c^2. \quad (14)$$

In the underdetermined case, it is computationally advantageous to evaluate the right singular vectors and values of  $\underline{L} = \underline{U} \underline{\Sigma} \underline{V}^T$ , and exploit  $\underline{L}^T \underline{L} = \underline{V} \underline{\Lambda} \underline{V}^T$ , where  $\underline{\Lambda} = \underline{\Sigma}^T \underline{\Sigma}$ , together with the matrix inverse lemma to obtain

$$(\mu \underline{I} + \underline{L} \underline{L}^T)^{-1} = \frac{1}{\mu} (\underline{I} - \underline{L} \underline{V} (\mu \underline{I} + \underline{\Lambda})^{-1} \underline{V}^T \underline{L}^T$$

and thus

$$\underline{a} = -\underline{L} \underline{V} (\mu \underline{I} + \underline{\Lambda})^{-1} \underline{V}^T \underline{x} \quad (15)$$



$$\underline{a}^T \underline{a} = \underline{x}^T \mathbf{V}(\mu \mathbf{I} + \mathbf{\Lambda})^{-1} \mathbf{\Lambda}(\mu \mathbf{I} + \mathbf{\Lambda})^{-1} \mathbf{V}^T \underline{x} \leq c^2 \quad (16)$$

$$\hat{\underline{x}} = \mu \mathbf{V}(\mu \mathbf{I} + \mathbf{\Lambda})^{-1} \mathbf{V}^T \underline{x}. \quad (17)$$

Thus, the following procedure implements the ASR algorithm efficiently for the underdetermined case where  $M \geq 2N$ . Note that the output is zero whenever the constraint is inactive.

1. evaluate SVD (right singular vectors only) of  $\mathbf{L} = \mathbf{U}\mathbf{\Sigma}\mathbf{V}^T$ , note  $\mathbf{L}^T \mathbf{L} = \mathbf{V}\mathbf{\Sigma}^T \mathbf{\Sigma} \mathbf{V}^T = \mathbf{V}\mathbf{\Lambda}\mathbf{V}^T$
2. project data onto right singular vectors,  $\underline{\omega} = \mathbf{V}^T \underline{x}$
3. evaluate Lagrange multiplier  $\mu$  by solving  $\sum_{n=1}^{2N} \frac{\lambda_n \omega_n^2}{(\mu + \lambda_n)^2} \leq c^2$
4. evaluate output,  $\hat{\underline{x}} = \underline{0}$  if  $\mu = 0$ ,  $\hat{\underline{x}} = \mu \mathbf{V}(\mu \mathbf{I} + \mathbf{\Lambda})^{-1} \underline{\omega}$  otherwise

Evaluating the SVD in step (1) dominates the computational complexity of the underdetermined ASR algorithm.

In the overdetermined case, it is computationally advantageous to evaluate the eigen decomposition of  $\mathbf{L}\mathbf{L}^T = \mathbf{U}\mathbf{\Lambda}\mathbf{U}^T$  to obtain  $(\mu \mathbf{I} + \mathbf{L}\mathbf{L}^T)^{-1} = \mathbf{U}(\mu \mathbf{I} + \mathbf{\Lambda})^{-1} \mathbf{U}^T$  and thus

$$\underline{a} = -\mathbf{U}(\mu \mathbf{I} + \mathbf{\Lambda})^{-1} \mathbf{U}^T \mathbf{L} \underline{x} \quad (18)$$

$$\underline{a}^T \underline{a} = \underline{x}^T \mathbf{L}^T \mathbf{U}(\mu \mathbf{I} + \mathbf{\Lambda})^{-2} \mathbf{U}^T \mathbf{L} \underline{x} \leq c^2 \quad (19)$$

$$\hat{\underline{x}} = \underline{x} - \mathbf{L}^T \mathbf{U}(\mu \mathbf{I} + \mathbf{\Lambda})^{-1} \mathbf{U}^T \mathbf{L} \underline{x} \quad (20)$$

Thus, the following procedure implements the ASR algorithm efficiently for the overdetermined case where  $M < 2N$ .

1. evaluate eigen decomposition of  $\mathbf{L}\mathbf{L}^T = \mathbf{U}\mathbf{\Lambda}\mathbf{U}^T$
2. project lags onto eigenvectors,  $\mathbf{Q} = \mathbf{U}^T \mathbf{L}$
3. evaluate  $\underline{\omega} = \mathbf{Q} \underline{x}$
4. evaluate Lagrange multiplier  $\mu$  by solving  $\sum_{n=1}^{2N} \frac{\omega_n^2}{(\mu + \lambda_n)^2} \leq c^2$
5. evaluate output,  $\hat{\underline{x}} = \underline{x} - \mathbf{Q}^T (\mu \mathbf{I} + \mathbf{\Lambda})^{-1} \underline{\omega}$

Projecting the lags onto the eigenvectors, step (2), dominates the computational complexity of the overdetermined ASR algorithm

To apply the ASR algorithm to 2-D SAR data, we have two options. First, we can implement distinct 1-D ASR filters to the rows, then columns, or columns, then rows of an image, and select the ordering that achieves the

minimum output energy. This approach yields a sub-optimum (but very good) separable 2-D ASR filter. Finding the optimum separable ASR filter involves solving a set of nonlinear equations, and is difficult. The second option is to implement a nonseparable 2-D ASR filter. To preserve the computational simplicity and spirit of the 1-D ASR algorithm, we employ 2-D weighting functions of the form

$$A(n_x, n_y, k_x, k_y) = 1 + \sum_{\substack{m_x=0 \\ (m_x=m_y \neq 0)}}^M \sum_{m_y=0}^M a(n_x, n_y, m_x, m_y) \cos\left(\frac{2\pi m_x k_x}{K_x}\right) \cos\left(\frac{2\pi m_y k_y}{K_y}\right). \quad (21)$$

In this manner, we obtain a 2-D FIR filter implementation. However, since the weights are nonseparable functions of the 2-D lags, we do not encounter non-linear equations in solving for the filter coefficients. In fact, by defining  $M(M+2)$ -element vectors in the obvious way, the formalism of our 1-D solutions can be used directly to obtain a 2-D solution. For a given order  $M$ , the separable ASR filter offers  $M$  degrees of freedom in each direction, while the nonseparable ASR filter offers a total of  $M(M+2)$  degrees of freedom.

A simple argument establishes the minimum constraint value that will insure that the input sinc IPR sidelobes are eliminated in the ASR output image. We consider the simplified case of a single isolated sinc IPR input to the scalar ASR algorithm. Without loss of generality, we can assume that the input sinc IPR is real-valued. Under these conditions, the ASR filter vector is simply proportional to the lag vector, i.e.  $\underline{a} = -\alpha \underline{l}$ , so  $\hat{x} = x - \alpha \underline{l}^T \underline{l}$ . For both separable and nonseparable ASR implementations, the most challenging sidelobe reduction problem is to eliminate the distant on-axis sidelobes of the separable sinc IPR. Assume that we seek to eliminate the  $n^{th}$  distant sidelobe of a unit-amplitude sinc IPR, with value  $x \approx \frac{(-1)^n}{2n\pi}$ . For small filter orders ( $M \ll n$ ) the  $M(M+2)$  nonseparable lags are approximately  $\underline{l}_{ns}^T = (\frac{(-1)^{n+1}}{2n\pi}, \dots, \frac{(-1)^{n+M}}{2n\pi}, 0, \dots, 0)$ ; only  $M$  of them are non-zero. Similarly, the  $M$  separable lags are approximately  $\underline{l}_{sep}^T = (\frac{(-1)^{n+1}}{2n\pi}, \dots, \frac{(-1)^{n+M}}{2n\pi})$ . In either case,  $\underline{l}^T \underline{l} = \frac{M}{(2n\pi)^2}$ , and requiring the output to be zero requires  $\alpha = \frac{2n\pi}{M}$ . Thus we find that  $\underline{a}^T \underline{a} = \alpha^2 \underline{l}^T \underline{l} = 1/M$ , which suggests that using a filter constraint of  $c = 1/\sqrt{M}$  will eliminate sidelobes.

Similarly, we examine the scalar case of a single point-scatterer in white Gaussian noise to understand the impact of ASR order and constraint on TCR. In this case, the input to ASR is a single isolated sinc IPR embedded in interpolated white Gaussian noise. We assume that the sinc IPR is centered on one of the sample points so that when ASR filters the pixel where the target is located, the target does not contribute to any of the lags used by the ASR filter. We assume further that the amplitude of the target sinc IPR to be a circular Gaussian random variable with variance  $\sigma_t^2$ , and that the circular noise/clutter variance is  $\sigma_c^2$ ; in both cases the variances of the I and Q channels are half as large.

Our TCR analysis establishes the variances of *underdetermined* ASR outputs corresponding to target and (distant) clutter, and compares them against the input variances. We define the TCR gain afforded by ASR as the ratio of

output to input TCR, i.e.

$$\beta = \frac{\left( \frac{E(\hat{\mathbf{x}}^T \hat{\mathbf{x}} | \text{target})}{E(\hat{\mathbf{x}}^T \hat{\mathbf{x}} | \text{clutter})} \right)}{\left( \frac{E(\mathbf{x}^T \mathbf{x} | \text{target})}{E(\mathbf{x}^T \mathbf{x} | \text{clutter})} \right)}.$$

Note that this gain factor does not include (or is in addition to) the Fourier compression gain that arises in transforming from the signal history to image domain.

For both target and clutter pixels, the output variance can be expressed in terms of the conditional variances given that the Lagrange multiplier is or is not active, weighted by the associated probabilities, i.e.

$$E(\hat{\mathbf{x}}^T \hat{\mathbf{x}}) = E(\hat{\mathbf{x}}^T \hat{\mathbf{x}} | \mu = 0)P(\mu = 0) + E(\hat{\mathbf{x}}^T \hat{\mathbf{x}} | \mu > 0)P(\mu > 0) = E(\hat{\mathbf{x}}^T \hat{\mathbf{x}} | \mu > 0)P(\mu > 0) \quad (22)$$

where we have used the fact that the underdetermined ASR output is zero when the constraint is inactive. The probability that the constraint is active is

$$P(\mu > 0) = P\left(\sum_{n=1}^2 \frac{\omega_n^2}{\lambda_n} > c^2\right) = 1 - P\left(\sum_{n=1}^2 \frac{\omega_n^2}{\lambda_n} \leq c^2\right). \quad (23)$$

While  $\underline{\omega} = \mathbf{V}\underline{x}$  is a vector of independent Gaussian random variables, just like  $\underline{x}$  (since  $\mathbf{V}$  is unitary), the eigenvalues  $\Lambda$  of  $\mathbf{L}^T \mathbf{L}$  are random. Although  $\{\omega_n\}$  and  $\{\lambda_n\}$  are independent, the presence of the random eigenvalues complicates the evaluation of the distribution, probability (23), and subsequent analysis. Therefore, we make the simplifying asymptotic (large filter order) assumption that

$$\mathbf{L}^T \mathbf{L} \longrightarrow \mathcal{M} \frac{\sigma_c^2}{2} \mathbf{I} \text{ and } \lambda_n \longrightarrow \mathcal{M} \frac{\sigma_c^2}{2},$$

which is justified by the fact that, at both target and (distant) clutter pixels, the lags consist of white Gaussian noise with component variance  $\sigma_c^2/2$ . The number of adaptive degrees of freedom,  $\mathcal{M}$ , which factors into the asymptotic eigenvalues, is different for the nonseparable and separable cases:

$$\mathcal{M} = \begin{cases} M(M+2) & (\text{nonseparable}) \\ M & (\text{separable}). \end{cases} \quad (24)$$

Then, noting that for target (variance  $\sigma_t^2$ ) and clutter (variance  $\sigma_c^2$ ) pixels, respectively,  $Y \equiv \sum_{n=1}^2 \frac{2}{\sigma_{t,c}^2} \omega_n^2$  is a unit  $\chi^2$  random variable with two degrees of freedom, and density  $p_Y(y) = \frac{1}{2} e^{-y/2} u(y)$ , we can rewrite (23) as

$$P(\mu > 0) = 1 - P(Y \leq \mathcal{M} c^2 \frac{\sigma_c^2}{\sigma_{t,c}^2}) = e^{-\frac{\mathcal{M} c^2}{2} \frac{\sigma_c^2}{\sigma_{t,c}^2}}. \quad (25)$$

When the Lagrange multiplier is active, we require

$$\underline{a}^T \underline{a} = \sum_{n=1}^2 \frac{\lambda_n \omega_n^2}{(\mu + \lambda_n)^2} = \frac{\mathcal{M} \frac{\sigma_c^2 \sigma_{t,c}^2}{2}}{(\mu + \mathcal{M} \frac{\sigma_c^2}{2})^2} y = c^2,$$

which leads to

$$\mu = \frac{1}{2} \left( \frac{\sqrt{\mathcal{M}}}{c} \sigma_c \sigma_{t,c} X - \mathcal{M} \sigma_c^2 \right), \quad (26)$$

where  $X \equiv \sqrt{Y}$  is a unit  $\chi$  random variable with two degrees of freedom and density  $p_X(x) = x e^{-x^2/2} u(x)$ . Note that the condition when the constraint is active, i.e.  $\mu > 0$ , occurs when  $X > \sqrt{\mathcal{M} c^2 \frac{\sigma_c^2}{\sigma_{t,c}^2}}$ . The ASR output energy is

$$\hat{\underline{x}}^T \hat{\underline{x}} = \sum_{n=1}^2 \frac{\mu^2 \omega_n^2}{(\mu + \lambda_n)^2} = \frac{\mu^2}{(\mu + \mathcal{M} \frac{\sigma_c^2}{2})^2} X^2,$$

which, combined with equation (26) yields

$$\hat{\underline{x}}^T \hat{\underline{x}} = \frac{\sigma_{t,c}^2}{2} \left( X - \sqrt{\mathcal{M} c^2 \frac{\sigma_c^2}{\sigma_{t,c}^2}} \right)^2.$$

Consequently, the variance of the ASR output given that the constraint is active is

$$\begin{aligned} E(\hat{\underline{x}}^T \hat{\underline{x}} | \mu > 0) &= \frac{\sigma_{t,c}^2}{2} \int_{\sqrt{\mathcal{M} c^2 \frac{\sigma_c^2}{\sigma_{t,c}^2}}}^{\infty} \left( X - \sqrt{\mathcal{M} c^2 \frac{\sigma_c^2}{\sigma_{t,c}^2}} \right)^2 p_X(x) dx \\ &= \sigma_{t,c}^2 \left( e^{-\frac{\mathcal{M} c^2}{2} \frac{\sigma_c^2}{\sigma_{t,c}^2}} - \sqrt{\frac{\mathcal{M} c^2}{2} \frac{\sigma_c^2}{\sigma_{t,c}^2}} \sqrt{\pi} (1 - \text{erf}(\sqrt{\frac{\mathcal{M} c^2}{2} \frac{\sigma_c^2}{\sigma_{t,c}^2}})) \right). \end{aligned} \quad (27)$$

Substituting equations (25) and (27) into (22) yields the output variance of the underdetermined ASR filter:

$$E(\hat{\underline{x}}^T \hat{\underline{x}}) = \sigma_{t,c}^2 e^{-\frac{\mathcal{M} c^2}{2} \frac{\sigma_c^2}{\sigma_{t,c}^2}} \left( e^{-\frac{\mathcal{M} c^2}{2} \frac{\sigma_c^2}{\sigma_{t,c}^2}} - \sqrt{\frac{\mathcal{M} c^2}{2} \frac{\sigma_c^2}{\sigma_{t,c}^2}} \sqrt{\pi} (1 - \text{erf}(\sqrt{\frac{\mathcal{M} c^2}{2} \frac{\sigma_c^2}{\sigma_{t,c}^2}})) \right). \quad (28)$$

Using equations (28) for the target and clutter output variances, we find that the TCR gain is a function of the product of number of adaptive degrees of freedom and the squared-constraint, and the input TCR:

$$\beta = g(\mathcal{M} c^2, \frac{\sigma_t^2}{\sigma_c^2}) = \frac{e^{-\frac{\mathcal{M} c^2}{2} \frac{\sigma_c^2}{\sigma_t^2}} \left( e^{-\frac{\mathcal{M} c^2}{2} \frac{\sigma_c^2}{\sigma_t^2}} - \sqrt{\frac{\mathcal{M} c^2}{2} \frac{\sigma_c^2}{\sigma_t^2}} \sqrt{\pi} (1 - \text{erf}(\sqrt{\frac{\mathcal{M} c^2}{2} \frac{\sigma_c^2}{\sigma_t^2}})) \right)}{e^{-\frac{\mathcal{M} c^2}{2}} \left( e^{\frac{\mathcal{M} c^2}{2}} - \sqrt{\frac{\mathcal{M} c^2}{2}} \sqrt{\pi} (1 - \text{erf}(\sqrt{\frac{\mathcal{M} c^2}{2}})) \right)}. \quad (29)$$

As a function of increasing input TCR, the gain function saturates at a value dictated purely by the product  $\mathcal{M} c^2$ , i.e.

$$\beta_{\max} = \frac{1}{e^{-\frac{\mathcal{M} c^2}{2}} \left( e^{\frac{\mathcal{M} c^2}{2}} - \sqrt{\frac{\mathcal{M} c^2}{2}} \sqrt{\pi} (1 - \text{erf}(\sqrt{\frac{\mathcal{M} c^2}{2}})) \right)}. \quad (30)$$

For a nonseparable ASR filter the TCR gain is, directly

$$\beta_{nonsep} = g(M(M+2)c^2, \frac{\sigma_t^2}{\sigma_c^2}). \quad (31)$$

On the other hand, for a separable ASR filter, we get a cascade of gain from running in the row and column directions

$$\beta_{sep} = g(Mc^2, \frac{\sigma_t^2}{\sigma_c^2} g(Mc^2, \frac{\sigma_t^2}{\sigma_c^2})). \quad (32)$$

Equations (31) and (32) suggest that underdetermined nonseparable and separable ASR filters for which the product of degrees-of-freedom and squared-constraint is a constant, i.e.  $\mathcal{E} = Mc^2$ , offer the same peak level of TCR gain; however, since the separable ASR filter cascades these gains, it attains high levels of gain at lower input TCR than the nonseparable ASR filter. Figure 3 illustrates theoretically predicted and observed TCR gain vs. input TCR for nonseparable and separable filters using  $\mathcal{E} = 1$  and  $\mathcal{E} = 2$ . While the TCR gain predicted theoretically is higher than observed in practice, the predictions accurately reflect the general behavior with respect to order, constraint, and input TCR that we observe empirically from synthetic point targets imbedded in white Gaussian noise. Thus our theoretical TCR gain model affords useful insight.

Table 2 summarizes strategies to select ASR constraint to either eliminate sidelobes or improve peak TCR by a fixed gain as a function of filter order and nonseparable or separable implementation. Note that the separable sidelobe and TCR gain strategies are consistent, in that they share the same power-of-order dependence. This is not surprising, given the separable nature of the input sinc IPR. In contrast, the nonseparable sidelobe strategies are not compatible. If one implements the sidelobe rejection strategy with both nonseparable and separable filters, the nonseparable filter will, theoretically, provide more peak TCR gain,

$$\left. \frac{\beta_{max}^{ns}}{\beta_{max}^{sep}} \right|_{c=1/\sqrt{M}} = \frac{e^{-\frac{1}{2}} \left( e^{-\frac{1}{2}} - \sqrt{\frac{1}{2}} \sqrt{\pi} (1 - \text{erf}(\sqrt{\frac{1}{2}})) \right)}{e^{-\frac{M+2}{2}} \left( e^{\frac{M+2}{2}} - \sqrt{\frac{M+2}{2}} \sqrt{\pi} (1 - \text{erf}(\sqrt{\frac{M+2}{2}})) \right)}. \quad (33)$$

Implementation	Eliminate Sidelobes	Control Overdetermined Peak TCR Gain
nonseparable	$c = \frac{1}{\sqrt{M}}$	$c = \sqrt{\frac{\mathcal{E}}{M(M+2)}}$
separable	$c = \frac{1}{\sqrt{M}}$	$c = \sqrt{\frac{\mathcal{E}}{M}}$

Table 2: Strategies to select ASR constraint vs. order to either eliminate sidelobes or achieve specified peak TCR gain.

### 2.1.6 SVA

The space-variant apodization (SVA) algorithm is a special case of ASR that exhibits minimal impact on clutter. Its dominant impact is to remove the sinc sidelobe artifacts present in unweighted Fourier imagery. SVA exploits a separable ASR filter of order one (hence overdetermined even for a single channel) together with a filter coefficient positivity constraint. This constraint reflects the oscillatory nature of a sinc IPR. When the pixel being operated upon is a sidelobe of sinc IPR, the neighboring lags are of opposite sign, and adding them to (rather than subtracting them from) the input reduces the output energy. An additional ramification of this constraint is that it prevents SVA from sharpening the interpolated sinc mainlobe, since in this case the neighboring lags share the sign of the mainlobe, and a negative coefficient is necessary to reduce the output energy. Since the SVA algorithm uses only a single filter coefficient, it is more direct to employ complex notation rather than the separate I/Q channel notation employed in deriving the higher-order ASR algorithm.

While the SVA algorithm typically utilizes a constraint value of  $c = 1$ , here we provide the explicit formulation of SVA for arbitrary positive  $c$ . As with the ASR notation, we suppress the understood dependence on spatial location  $r$ . Multi-channel SVA evaluates  $\hat{x} = x + al$ , where each element of lag vector  $l$  represents a single complex-valued lag, and minimizes the output energy with respect to  $a$  subject to the dual constraints  $a^2 < c^2$  and  $a \geq 0$ . Using the method of Lagrange multipliers, the solution is obtained via the following procedure:

1. evaluate unconstrained solution  $a_u = -\frac{\text{Re}(x^H l)}{l^H l}$
2. evaluate output
  - if  $a_u \leq 0$  then use  $a = 0$  and  $\hat{x} = x$
  - else if  $a_u^2 \leq c^2$  use  $a = a_u$  and  $\hat{x} = x - \frac{\text{Re}(x^H l)}{l^H l} l$
  - else use  $a = c$  and  $\hat{x} = x + cl$ .

The computational burden of the SVA algorithm is trivial, being dominated by evaluating the dot products  $x^H l$  and  $l^H l$  in step 1.

### 2.1.7 Auto-Regressive Linear Prediction

Auto-regressive linear prediction methods predict a particular sample  $P$  in the signal history subaperture as a linear combination of the remaining samples, i.e.

$$\hat{X}_P = - \sum_{\substack{m=0 \\ m \neq P}}^{K-1} a_m^* X_m.$$

The prediction error is  $\epsilon_P = X_P - \hat{X}_P = \underline{A}_P^H \underline{X}$  where  $a_P \equiv 1$ , and  $\underline{A}_P$  is the *error* prediction filter. The error prediction coefficients are chosen to minimize the average prediction error energy over all subapertures within the

full signal history aperture,

$$E(|\underline{A}_P^H \underline{X}|^2) = \underline{A}_P^H \mathbf{R} \underline{A}_P, \quad (34)$$

subject to the constraint  $\underline{A}_P^H \underline{P} = a_P = 1$ , where  $\underline{P}$  is a vector of zeros, with a single unit-valued entry corresponding to the predicted element. Solving the constrained optimization via the method of Lagrange multipliers yields

$$\underline{A}_P = \frac{\mathbf{R}^{-1} \underline{P}}{\underline{P}^H \mathbf{R}^{-1} \underline{P}} \quad (35)$$

and a minimum prediction error energy of  $1/\underline{P}^H \mathbf{R}^{-1} \underline{P} = 1/R_{P,P}^{-1}$ .

One can invert the prediction process, and view the prediction error as noise driving an all-pole (auto-regressive) filter whose output is the data sample being predicted. Based on the assumption that the prediction error signal is an innovations process, i.e. white noise, the PSD estimate equals the minimized prediction error energy divided by the magnitude squared of the transfer function. However, it is known that the PSD should be chosen as the square root of this quantity to obtain correct scaling [6,12]. Thus, the ARLP spectral estimate is

$$S_{ARLP-P}(r) = \frac{\sqrt{R_{P,P}^{-1}}}{|\underline{P}^H \mathbf{R}^{-1} \underline{W}(r)|}. \quad (36)$$

Evaluating and inverting the correlation matrix  $\mathbf{R}$  (or at least solving the equations  $\mathbf{R} \underline{A}_P = \underline{P}$ ) dominates the computational complexity of ARLP.

A more common, but equivalent formulation of the ARLP algorithm involves solving the normal equations

$$\mathcal{R}_P \underline{A}_P = -\underline{r}_P^*$$

where the reduced correlation matrix  $\mathcal{R}_P$  is obtained from the full correlation matrix  $\mathbf{R}$  by omitting prediction element row and column  $P$ , and  $\underline{r}_P$  is obtained by extracting column  $P$  from the full correlation matrix, omitting the  $P^{th}$  row. Similarly, the prediction filter  $\underline{A}_P$  is missing the  $P^{th}$  unit entry element of the error prediction filter  $\underline{A}_P$ . One reason for the popularity of this less conceptually direct formulation is that, in the special case of Toeplitz correlation estimates (correlation method) and a causal prediction filter, the normal equations become the Yule-Walker equations, which make the use of efficient numerical methods, such as Durbin's recursion, more direct. In addition, the normal equation formulation is useful for describing the Tufts-Kumaresan ARLP algorithm.

### 2.1.8 ARLP Spectral Averaging and Pisarenko's Method

The signal history sample  $P$  being predicted need not have any particular ordinal relation to the samples being used to predict it. In other words, the filter need not be causal, semi-causal, etc. ARLP imagery based on any one choice

of prediction element may exhibit spurious spiky behavior and elliptical, rather than circular, contours. While our experience does not suggest any reason to prefer one choice over another, we have found it essential to use an average ARLP image based on multiple (at least two) ARLP images based on different prediction elements. In particular, the first- and second-quadrant averaging proposed in [26] reduces, but does not eliminate, the spurious spikiness and makes the countours more circular:

$$S_{ARLP-pair}(r) = \frac{1}{\sqrt{\frac{[\underline{P}^H \mathbf{R}^{-1} \underline{W}(r)]^2}{R_{P,P}^{-1}} + \frac{[\underline{P}_\perp^H \mathbf{R}^{-1} \underline{W}(r)]^2}{R_{P_\perp, P_\perp}^{-1}}}}$$

In this case prediction elements  $P$  and  $P_\perp$  are chosen such that they lie in orthogonal quadrants with respect to the center of the subaperture. Even with this averaging, the choice of “best” orthogonal prediction element spectra to average remains unanswered. A logical generalization of the orthogonal-quadrant averaging concept is to RMS average inverse ARLP spectra/images across all possible prediction elements, i.e.

$$\begin{aligned} S_{RMS-ARLP}(r) &= \frac{1}{\sqrt{\sum_P \frac{1}{R_{P,P}^{-1}} \underline{W}^H(r) \mathbf{R}^{-1} P P^H \mathbf{R}^{-1} \underline{W}(r)}} \\ &= \frac{1}{\sqrt{\underline{W}^H(r) \mathbf{R}^{-1} (\text{diag}(\mathbf{R}^{-1}))^{-1} \mathbf{R}^{-1} \underline{W}(r)}}, \end{aligned}$$

where  $\text{diag}(\mathbf{R}^{-1})$  indicates the diagonal portion of  $\mathbf{R}^{-1}$ , so  $((\mathbf{R}^{-1}))^{-1}$  is a diagonal matrix of prediction errors.

If one makes the generally invalid assumption that the individual ARLP filters yield the same prediction error energy, i.e.  $R_{P,P}^{-1} \equiv \epsilon^2$ , then the RMS ARLP image reduces to one of a family of estimates suggested by Pisarenko [9]:

$$S_{RMS-ARLP}(r) \rightarrow \frac{\epsilon}{\sqrt{\underline{W}^H(r) \mathbf{R}^{-2} \underline{W}(r)}} = S_{PISARENKO}(r). \quad (37)$$

In practice, the differences between RMS ARLP imagery and Pisarenko imagery are negligible.

### 2.1.9 Signal-Noise Subspace Decomposition

Here we consider the idealized form and properties of the signal history correlation matrix based on an assumption of a superposition of sinusoids (point scatterers) embedded in additive white Gaussian noise,

$$\underline{X} = \underbrace{\sigma_o \underline{N}}_{\text{white noise}} + \underbrace{\sum_{l=1}^L \sigma_l \underline{W}(r_l)}_{L \text{ sinusoids}} = \sigma_o \underline{N} + \mathbf{Q} \underline{\sigma} \quad \text{where} \quad \mathbf{Q} = (\underline{W}(r_1) \cdots \underline{W}(r_L)).$$



The ideal (infinite averaging) correlation matrix takes the form of an identity matrix scaled by the noise variance, combined with a quadratic term that combines outer-products of  $L$  constituent sinusoidal signal vectors weighted by a so-called coherence matrix,

$$\mathbf{R} = \sigma_o^2 \mathbf{I} + \mathbf{Q} E(\underline{\sigma} \underline{\sigma}^H) \mathbf{Q}^H = \sigma_o^2 \mathbf{I} + \mathbf{Q} \mathbf{C} \mathbf{Q}^H.$$

The diagonal terms of the coherence matrix  $\mathbf{C}$  are the sinusoid energies. By definition, the correlation matrix is positive definite and Hermitian; consequently, its eigenvectors form an orthonormal basis for the  $\hat{K}$ -dimensional space spanned by its columns. Further, the correlation matrix can be expressed as a sum of outer-products of the eigenvectors weighted by their associated eigenvalues. The  $L$  eigenvectors associated with the largest eigenvalues span the subspace defined by the sinusoid vectors, i.e. the columns of the signal matrix  $\mathbf{Q}$ . The remaining  $\hat{K} - L$  eigenvectors are orthogonal to the signal vectors, and display eigenvalues equal to the noise variance. The signal subspace eigenvalues are larger than the noise variance, but their values are complicated functions of the point scattering energies and differential locations.

$$\mathbf{R} = \sum_{\text{noise}} \lambda_m \underline{V}_m \underline{V}_m^H + \sum_{\text{signal}} \lambda_m \underline{V}_m \underline{V}_m^H = \sum_{\text{noise}} \sigma_o^2 \underline{V}_m \underline{V}_m^H + \sum_{\text{signal}} \lambda_m \underline{V}_m \underline{V}_m^H.$$

The correlation matrix inverse can be expressed similarly, but with the eigenvalues reciprocated.

$$\mathbf{R}^{-1} = \sum_{\text{noise}} \sigma_o^{-2} \underline{V}_m \underline{V}_m^H + \sum_{\text{signal}} \lambda_m^{-1} \underline{V}_m \underline{V}_m^H.$$

Based on this ideal model, it would seem that one could determine the order  $L$ , i.e. the number of point scatterers, simply by recognizing the number of eigenvalues that are not equal. In practice, our correlation matrix estimate is imperfect, and statistical perturbations cause the noise eigenvalues to deviate about the noise energy. A collection of  $L$  equal energy scatterers typically produces a range of signal eigenvalues, that can vary from near the noise energy to well above it. Thus, establishing the order is not as simple as one would like. There are two simple methods for establishing the model order. First, one can assume the value of  $L$  *a-priori*, and assume that the largest eigenvalues correspond to the point scatterers. Second, one can assume that the ensemble of point scatterers contributes a fixed fraction  $f$  of the total signal history; the order is selected so that  $\sum_{m=\hat{K}-L}^{\hat{K}} \lambda_m = f \sum_{m=1}^{\hat{K}}$ . More complicated order selection criteria exist. We defer further discussion of order selection until we show examples with actual SAR data.

### 2.1.10 Eigenvector and MUSIC

Based on our subspace decomposition discussion, one can view the eigenvector and MUSIC methods as perturbations of MVM that seek to drive the denominator toward zero when the analysis sinusoid vector  $\underline{W}$  aligns with one of the true sinusoid vectors, thereby giving rise to sharp and high spectral peaks. Since the correlation matrix eigenvectors

that span the noise subspace are orthogonal to the signal vectors, EV and MUSIC retain, in their expression for the correlation matrix inverse, only those eigenvector outer products that lie in the noise subspace. While EV reciprocates the measured noise eigenvalues, MUSIC exploits the white noise model further, by replacing the measured noise eigenvalues with a constant (we use the arithmetic mean of the measured noise eigenvalues).

$$S_{EV}(r) = \frac{1}{\underline{W}^H(r) \left( \sum_{\text{noise}} \lambda_m^{-1} \underline{V}_m \underline{V}_m^H \right) \underline{W}(r)} = \frac{1}{\sum_{\text{noise}} \lambda_m^{-1} |\underline{W}^H(r) \underline{V}_m|^2}. \quad (38)$$

$$S_{MUSIC}(r) = \frac{1}{\underline{W}^H(r) \left( \sum_{\text{noise}} \sigma_o^{-2} \underline{V}_m \underline{V}_m^H \right) \underline{W}(r)} = \frac{1}{\sum_{\text{noise}} \sigma_o^{-2} |\underline{W}^H(r) \underline{V}_m|^2}. \quad (39)$$

Evaluating and performing the eigen decomposition of the correlation matrix  $\mathbf{R}$  dominates the computational complexity of EV and MUSIC; subsequent evaluation of the quadratic form in equation (38) or (39) involves computing a pair of 2-D FFTs.

#### 2.1.11 Tufts-Kumaresan ARLP

Based on our subspace decomposition discussion, one can view the Tufts-Kumaresan method as a perturbation of ARLP that seeks to drive the denominator toward zero when the analysis sinusoid vector  $\underline{W}$  aligns with one of the true sinusoid vectors, by forcing the error prediction filter to lie in the noise subspace.

The Tufts-Kumaresan algorithm differs from conventional linear prediction in two respects. First, it allows the use of larger subapertures, such that the correlation matrix becomes singular, by employing the Moore-Penrose pseudoinverse in calculating the prediction filter. Use of larger subapertures improves resolution. Second, the correlation matrix is truncated to omit the noise contribution. This truncation improves the apparent SNR. Thus, the TK-ARLP prediction filter is the minimum-norm solution to

$$\mathcal{R}_{P;sig} \underline{A}_P = -\underline{r}_P^*,$$

which is

$$\underline{A}_P = -\mathcal{R}_{P;sig}^\dagger \underline{r}_P^* = - \sum_{\text{signal}} \lambda_m^{-1} \underline{V}_m \underline{V}_m^H \underline{r}_P^*. \quad (40)$$

One obtains the corresponding error prediction filter  $\underline{A}_P$  by inserting a one in the  $P^{th}$  entry of the prediction filter  $\underline{A}_P$ , and obtains the TKARLP image

$$S_{TKARLP-P}(r) = \frac{1}{|\underline{A}_P^H \underline{W}(r)|}. \quad (41)$$

Evaluating and performing the eigen decomposition of the correlation matrix  $\mathcal{R}_P$ , or the SVD of the corresponding forward-backward subaperture data matrix dominates the computational complexity of TKARLP. As with ARLP, we find that TKARLP works best when some form of RMS averaging of imagery based on multiple prediction elements is performed.

### 2.1.12 Parametric Maximum Likelihood

The PML algorithm fits a complex-valued superposition of sinusoids to the signal history data, and selects the amplitude, phase, and range of the point scatterers to minimize residual energy. For sinusoids in white Gaussian noise, the PML algorithm achieves the Cramer-Rao lower bound on estimation accuracy. The signal model is

$$\underline{X} = \sigma_o \underline{N} + \underline{Q} \underline{\sigma} \quad \text{where} \quad \underline{Q} = (\underline{W}(r_1) \cdots \underline{W}(r_L)),$$

while the estimated signal model is

$$\hat{\underline{X}}(\hat{\underline{\sigma}}, \hat{\underline{r}}) = \hat{\underline{Q}} \hat{\underline{\sigma}} \quad \text{where} \quad \hat{\underline{Q}} = (\underline{W}(\hat{r}_1) \cdots \underline{W}(\hat{r}_L))$$

The residual and its energy are

$$\underline{\epsilon}(\hat{\underline{\sigma}}, \hat{\underline{r}}) = \underline{X} - \hat{\underline{X}}(\hat{\underline{\sigma}}, \hat{\underline{r}})$$

$$P(\hat{\underline{\sigma}}, \hat{\underline{r}}) = \underline{\epsilon}^H \underline{\epsilon} = \underline{X}^H \underline{X} - \underline{X}^H \hat{\underline{Q}} \hat{\underline{\sigma}} - \hat{\underline{\sigma}}^H \hat{\underline{Q}}^H \underline{X} + \hat{\underline{\sigma}}^H \hat{\underline{Q}}^H \hat{\underline{Q}} \hat{\underline{\sigma}}$$

Given a set of point scattering location estimates, we minimize the residual energy with respect to the complex amplitudes via closed-form least-squares regression,

$$\hat{\underline{\sigma}}(\hat{\underline{r}}) = (\hat{\underline{Q}}^H \hat{\underline{Q}})^{-1} \hat{\underline{Q}}^H \underline{X},$$

which yields the residual which now must be minimized with respect to the spatial scattering locations:

$$P(\hat{\underline{r}}) = \underline{X}^H \underline{X} - \underline{X}^H \hat{\underline{Q}}^H (\hat{\underline{Q}}^H \hat{\underline{Q}})^{-1} \hat{\underline{Q}}^H \underline{X}.$$

We employ quasi-Newton methods to solve this nonlinear optimization problem [17] in conjunction with interactive graphics that lets us monitor and guide the convergence of the algorithm from a set of selectable initial location estimates.

## 2.2 Simulated Point-Scattering Results

Preliminary assessment of the benefits and limitations of 2-D spectral estimation algorithms for SAR imaging can be made using simulated point scatterers. These simple examples illustrate the characteristic properties of these imaging methods.

Figure 4 compares imagery of a collection of 36 equal-amplitude, randomly phased simulated point scatterers, configured to spell  $\Sigma$ ERIM, in additive white Gaussian noise/clutter; the Fourier image domain TCR is 33dB (the product of the 6dB signal history domain SNR and the 27dB compression gain afforded by the  $24 \times 24$  signal history sample size). This is a higher TCR than is typical of many SAR imaging scenarios. The SVA image essentially resembles sinc mainlobe contributions (from an unweighted Fourier image) of the point scatterers, and is sharper than the baseline Taylor-weighted Fourier imagery. The ASR and RRMVM images are slightly sharper than the SVA image, and have enhanced the TCR due to their singular nature. Use of 50% subaperture averaging in our MVM, EV, MUSIC, ARLP, and Pisarenko examples (60% for TKARLP) penalizes these algorithms with roughly 6dB loss of compression gain (TCR) compared to the Fourier transform. Nevertheless, the MVM image is much sharper than the Fourier image, and the speckle variability of the clutter background is reduced. EV and MUSIC improve upon the resolution of MVM and boost the apparent TCR, more than compensating for the 6dB up-front loss. While MUSIC yields a benign, flat background, EV clutter variations track those afforded by MVM. The ARLP image exhibits numerous spurious peaks in the clutter background (despite first- and second-quadrant averaging). The Pisarenko image exhibits fewer spurious clutter peaks and more accurate target peaks than the ARLP image. The Pisarenko image is slightly sharper than the MVM image, but its clutter variability is higher; Pisarenko clutter variations track those afforded by MVM. TKARLP provides excellent localization of the point scatterers, but loses roughly 20dB of TCR. PML provides extremely accurate estimates of point scattering amplitude, phase, and location, as is evident by comparing them against the true point locations and amplitudes. All of these methods, with the possible exception of ARLP, provide a truer picture of the underlying point scatterers than does the baseline Taylor-weighted Fourier image.

Figure 5 compares the same types of imagery of the same simulated point scatterers when the Fourier image domain TCR is 13dB, which is a more typical TCR than the 33dB of Figure 4. As is well-known, the resolution of the MVM, EV, MUSIC, ARLP, TKARLP and Pisarenko methods is coarser at lower SNR than at high SNR. In contrast, the resolution of ASR and RRMVM methods appears to be largely independent of SNR. With the TCR already low, the compression losses suffered by MVM, ARLP and TKARLP are problematic. The EV and MUSIC algorithms offer better contrast, but are beginning to place their 36 peaks in erroneous locations. Both ASR and RRMVM provide better definition of the points in the  $\Sigma$  and M than EV or MUSIC.

Both ASR and RRMVM tend to suppress clutter scattering, thereby relatively enhancing stronger scattering. In

contrast, EV enhances strong point scatterers, while leaving clutter scattering relatively unaffected. While neither ASR nor RRMVM offers the resolution enhancement that EV can at high TCR, our experience is that both are more robust than EV at low TCR. ASR enhances locally prominent scatterers over a spatial extent dictated by the order of ASR the filter. In contrast, RRMVM and EV enhance only the strongest scatterers in the scene.

The Tufts-Kumaresan ARLP and parametric maximum likelihood approaches provide the best localization of the point scatterers. Indeed, much literature exists to illustrate that they approach and/or attain the Cramer-Rao bound on estimation accuracy for sinusoids in white noise. However, neither is well suited nor intended for imaging realistically complicated scenes. Consequently, we omit these two algorithms from further discussion.

Table 3 summarizes the dominant order of computational complexity (for single channel data), SNR compression gain (single point scatterer or sinusoid vs. white noise), and advantages or disadvantages of the 2-D spectral estimation algorithms for SAR imaging.  $K_x$  and  $K_y$  are the sizes of the SAR signal history in the range and cross-range directions, while  $\hat{K}_x$  and  $\hat{K}_y$  are the sizes of the signal history subapertures used to compute the correlation matrix. For perspective,  $K_x K_y$  is often on the order of one million.  $A_x$  and  $A_y$  are small amounts of averaging in the range and azimuth directions, satisfying  $A_x = K_x - \hat{K}_x + 1 \ll \hat{K}_x$  and  $A_y = K_y - \hat{K}_y + 1 \ll \hat{K}_y$ . Recall that the computational burden of the order  $(\hat{K}_x \hat{K}_y)^3$  complexity algorithms can be reduced by employing a decimation and mosaicing strategy.

### 2.3 Collected Scalar SAR Results

Naturally, a more complete assessment of the benefits and limitations of 2-D spectral estimation algorithms for SAR imaging necessitates the use of collected data. Here, we utilize Ku-band data collected by the WL-ERIM DCS radar of two commercial ships docked near Toledo, OH, together with some calibration trihedrals. The same signal history, which affords a uniformly weighted (sinc IPR) Fourier image resolution of one meter, was used to produce all images shown. The rectangularly formatted signal history employed is  $402 \times 402$  samples. We computed the Fourier image using Taylor weighting (-35dB peak sidelobe, order 5) to control IPR sidelobes and a zero-pad factor of two. We computed the ASR image using  $2 = 4$  (which provides 6 2-D ASR filter taps) and a constraint  $c = 1/2$  from the sinc IPR Fourier image. We exploited signal history decimation and image mosaicing to compute MVM, ARLP, Pisarenko, and EV images based on 40% subaperture forward-backward averaging. Each decimated signal history aperture was  $50 \times 50$ ; the subaperture size was  $20 \times 20$ . The overall images were computed as mosaics of  $100 \times 100$  overlapping subimages. The final image sizes for all methods is  $800 \times 800$  samples, of which  $500 \times 600$  samples are shown.

Figure 6 illustrates the baseline Taylor-weighted Fourier image on a relative 60dB grayscale. Sidelobes are visible in the water from the trihedral near the water's edge. Also note the water tower in the center-top portion of the image; the tower lays over toward the radar, which is looking from the right. All subsequent images should be

Technique	Complexity	TCR Gain	Advantages	Disadvantages	Comments
FFT	$K_x K_y \log K_x K_y$	$K_x K_y$	simple	speckle ML/SL tradeoff	interferometric
ASR	$K_x K_y M^2$ (nonsep) $K_x K_y M$ (sep)	$\gg K_x K_y$ (underdet) $K_x K_y$ (overdet)	low SL and sharp ML improves TCR	speckle local WSS	interferometric
SVA	$K_x K_y$	$K_x K_y$	simple low SL with sinc ML	speckle	interferometric
periodogram	$(\hat{K}_x \hat{K}_y)^3$	$\hat{K}_x \hat{K}_y$	reduces speckle	poor resolution sidelobes	
RRMVM	$\hat{K}_x \hat{K}_y (A_x A_y)^2$	$\gg \hat{K}_x \hat{K}_y$	low SL and/or sharp ML improves TCR	global WSS choice of constraint consistency	interferometric
MVM	$(\hat{K}_x \hat{K}_y)^3$	$\hat{K}_x \hat{K}_y$	reduces speckle good resolution no sidelobes	computation TCR-dependent res.	interferometric
ARLP	$(\hat{K}_x \hat{K}_y)^3$	$\hat{K}_x \hat{K}_y$	good resolution reduces speckle	computation spiky, req. mult. pred. TCR-dependent res.	
Pisarenko	$(\hat{K}_x \hat{K}_y)^3$	$\hat{K}_x \hat{K}_y$	good resolution no sidelobes	computation TCR-dependent res.	
EV/MUSIC	$(\hat{K}_x \hat{K}_y)^3$	$> \hat{K}_x \hat{K}_y$	reduces speckle fine resolution no sidelobes	computation order selection TCR-dependent res	MUSIC whitening inappropriate
TKARLP	$(\hat{K}_x \hat{K}_y)^3$	$< \hat{K}_x \hat{K}_y$	fine resolution	computation order selection TCR-dependent res	restricted applicability
PML	$\hat{K}_x \hat{K}_y L^2$	NA	accurate parameter estimates	not suitable for imaging	restricted applicability

Table 3: Synopsis of 2-D spectral estimation algorithm complexity, SNR processing gain, advantages and disadvantages for SAR imaging.

compared against this baseline.

Figure 7 illustrates the MVM image on a relative 45dB scale. The reduced dynamic range (compared to the 60dB scale used for the Fourier image) was chosen to preserve the apparent contrast ratio. The reduced MVM compression gain afforded by the 40% subapertures accounts for 8dB of the difference; we hypothesize that motion compensation errors, i.e. along-track phase errors, together with MVM's increased sensitivity to such errors, accounts for the remaining 7dB loss in contrast. Aside from contrast, the differences between MVM and Fourier imagery are startling. First, MVM improves the sharpness of the trihedrals and resolution of detail on the ships, yet displays less IPR scintillation (breakup) along the continuous bulkheads and gunwales of the ships. Second, there are no sidelobe artifacts in the MVM image. Third, MVM reduces clutter speckle. The MVM image has a more "optical" quality than the Fourier image.

Figure 8 illustrates the RRMVM image, evaluated using a forward-backward subaperture size of 400 samples out of an aperture of 402 samples and a constraint of 1.002, on a relative 70dB scale. This example highlights a problem that can arise with the algorithm when a large dynamic range of scattering amplitudes exists within the scene. In this case, RRMVM eliminates much of the detail of the ships' structure between the bow and stern has been eliminated,

yet, at the same time, fails to eliminate the sidelobes of the bright trihedral scatterers. To first order, the effect of RRMVM is to threshold the uniformly-weighted (sinc IPR) Fourier image. RRMVM exhibits too many adaptive degrees of freedom for the small amount of averaging and highly singular correlation matrix employed. The result is global weak signal suppression. While this suppression can be reduced by using smaller subapertures, i.e. more averaging, RRMVM rapidly loses its computational advantage when a significant amount of averaging is done.

Figure 9 illustrates the nonseparable (order 2, constraint .5) ASR image on a relative 70dB grayscale. Sidelobes are no longer visible in the water from the trihedral near the water's edge despite the 10dB increased dynamic range of the ASR display. The trihedrals and prominent scatterers on the ships are more sharply defined. In addition the contrast of the trihedrals with respect to the surrounding clutter is improved by roughly 8dB, although the variance of the clutter speckle (on a dB scale) is increased. While ASR eliminates sidelobes without suppressing weak scatterers globally, it does suppress weak scatterers locally, on the scale of the FIR filter size. Clutter suppression, local weak signal suppression, and increased clutter speckle are related phenomena caused by the complete lack of averaging in the spectral estimate, despite the small number of adaptive degrees of freedom.

Figure 10 illustrates the SVA image on a relative 60dB grayscale. Sidelobes are no longer visible in the water from the trihedral near the water's edge, yet the trihedrals and prominent scatterers on the ships are more sharply defined. For comparison, Figure 11 illustrates the unweighted (sinc IPR) Fourier image on a relative 60dB grayscale. The dominant impact of SVA is to eliminate the sidelobe artifacts while leaving the sinc IPR mainlobe and clutter largely intact.

Figure 12 illustrates the ARLP image on a relative 35dB scale. The reciprocal of this image is the RMS average of two reciprocal ARLP images based on first- and second-quadrant predictors, as described in the text. The ARLP image looks qualitatively rather poor. Compared to the MVM image, the ARLP image offers less contrast and displays spurious diagonal texture (both caused by ubiquitous spurious peaks), and exhibits sidelobe-like artifacts that extend throughout the scene.

Figure 13 illustrates the Pisarenko image on a relative 35dB scale. Compared to the MVM image (Figure 7), Pisarenko loses roughly 10dB of compression gain or contrast. We suspect this occurs because Pisarenko is even more sensitive than MVM to along-track phase errors. Otherwise, there appears to be little difference between the Pisarenko and MVM imagery. However, by averaging over all possible ARLP predictors, the Pisarenko image greatly reduces the spurious diagonal texture and improves the contrast afforded by the ARLP image based on a pair of prediction elements.

Figure 14 illustrates the EV image on a relative 45dB scale. To establish the order, i.e. the number of point targets for each mosaic chip, we employed a simple energy-based criterion, wherein the order was chosen so that the sum of the signal (largest) correlation matrix eigenvalues equaled 90% of the sum of all the eigenvalues. Compared to the MVM image, EV gains roughly 5dB of contrast, and appears strikingly sharp. The EV image is pleasing in mosaic

chips that include either man-made objects or inhomogeneous clutter. In such cases the energy-based order selection criterion enhances prominent points and meaningful texture with respect to benign homogeneous regions, which are smoothed as with MVM. However, the EV image exacerbates random noise texture in mosaic chips comprised of homogeneous clutter; in such cases there are no dominant signal eigenvalues, yet certain eigenvalues are decreed to be signal, and EV enhances the associated points. Furthermore, the boundaries between the mosaic chips are clearly visible with EV. SAR target detection, target recognition, and scene analysis problems usually involve spatially distributed objects. Order selection criteria that are based solely on discontinuities in or thresholding of the eigenvalue spectrum fail to satisfy our desire to enhance scatterers on the basis of their local prominence or relative spatial position. Further, order selection is complicated by the arbitrary manner in which an object or terrain can span multiple mosaic chips. More sophisticated order selection criteria are necessary to fully realize the potential of EV for SAR imaging. The logical intersection between EV order selection and SAR target detection is very intriguing.

Figures 15 and 16 illustrate heavily interpolated slices through one of the trihedrals on the causeway, and facilitate comparison of the sharpness, but not strictly the resolution, afforded by each algorithm. Figure 15 demonstrates that SVA effectively yields a sinc IPR mainlobe while eliminating the sinc sidelobes. ASR realizes a slight sharpening of the sinc mainlobe, together with a reduction in the background clutter. Both SVA and ASR offer lower sidelobes and sharper mainlobe than the baseline Taylor-weighted imagery. Figure 16 demonstrates that MVM, EV, ARLP, and Pisarenko all produce 3dB peak widths that are roughly five times sharper than the sinc IPR mainlobe. The relatively poor contrast ratios, compared to MVM, exhibited in the EV, ARLP, and Pisarenko slices reflects the greater sensitivity of these algorithms to measurement phase errors.

### 3 Interferometric and Polarimetric MVM, RRMVM, and ASR

Based on our experiences with the adaptive imaging algorithms applied to scalar data, we chose to pursue development of multi-channel and interferometric versions of MVM, RRMVM, and ASR. Neither ARLP nor signal-noise subspace decomposition methods offers a plausible basis for improving interferometric height estimates. In contrast, the MVM, RRMVM and ASR algorithms do. Through a combination of interference nulling, resolution enhancement, and averaging, MVM, RRMVM, and ASR may offer improved interferometric height estimates than Fourier imaging, provided that the same processing is applied to both interferometric channels, thereby preserving coherent phase.

Interferometric SAR systems exploit vertically displaced apertures  $A$  and  $B$  to collect registered, phase coherent signal histories,  $\underline{X}_A$  and  $\underline{X}_B$ . Conventional interferograms are the product of the Fourier image from aperture  $A$  times the conjugate of the Fourier image from aperture  $B$ , i.e.  $\underline{W}^H(r)\underline{X}_A\underline{X}_B^H\underline{W}(r)$ . The magnitude of the interferogram corresponds to scattering intensity, while the phase is proportional to scattering height out of the



slant-plane. Figure 17 illustrates the geometric and conceptual basis of interferometric SAR imaging.

Thermal noise, which is independent for the two channels, together with unresolved scatterers and IPR sidelobe leakage, contributes to interferometric phase noise, thereby degrading the accuracy of interferometric height estimates. Generally, height accuracy improves with increasing SNR. Often, it is necessary to lowpass filter the interferogram image to reduce the phase/height noise associated clutter and target scattering. Filtering the interferogram, rather than the phase, weights strong scatterers with less phase noise more heavily than weak scatterers with more phase noise. Unfortunately, spatial averaging of conventional interferograms degrades resolution.

To apply MVM and RRMVM to interferometric and/or polarimetric data, we assume balanced and independent thermal noise levels for the two interferometric channels  $A$  and  $B$ . Consequently, we apply the same processing to channels  $A$  and  $B$ , and maximize SIR on the basis of the average of the two channels. Similarly, we assume that we seek a polarimetric span-like intensity which represents the average energy received by a receive antenna whose polarization is aligned with the scattered field, over all possible transmit polarizations. Thus we apply the same processing to all polarimetric channels, and maximize SIR on the basis of the average of the polarization channels. An average correlation matrix

$$\mathbf{R}_{avg} = (\mathbf{R}_{HH,AA} + \mathbf{R}_{HH,BB} + \mathbf{R}_{HV,AA} + \mathbf{R}_{HV,BB} + \mathbf{R}_{VH,AA} + \mathbf{R}_{VH,BB} + \mathbf{R}_{VV,AA} + \mathbf{R}_{VV,BB})/8 \quad (42)$$

across the interferometric and polarimetric channels arises naturally as we seek to minimize average output energy, or maximize average SIR. Thus, from equations (4) and (6), the interferometric and polarimetric MVM and RRMVM filters, respectively, are

$$\underline{A}(r) = \frac{\mathbf{R}_{avg}^{-1} \underline{W}(r)}{\underline{W}^H(r) \mathbf{R}_{avg}^{-1} \underline{W}(r)} \quad (43)$$

and

$$\underline{A}(r) = \frac{(\mu(r)\mathbf{I} + \mathbf{R}_{avg})^{-1} \underline{W}(r)}{\underline{W}^H(r) (\mu(r)\mathbf{I} + \mathbf{R}_{avg})^{-1} \underline{W}(r)}, \quad (44)$$

where the Lagrange multiplier solves

$$\frac{\underline{W}^H(r) (\mu(r)\mathbf{I} + \mathbf{R}_{avg})^{-2} \underline{W}(r)}{(\underline{W}^H(r) (\mu(r)\mathbf{I} + \mathbf{R}_{avg})^{-1} \underline{W}(r))^2} \leq \frac{c^2}{\hat{K}_x \hat{K}_y}. \quad (45)$$

In both cases, we average the output interferogram across all available subapertures (modified covariance method) to reduce noise and speckle, as well as all polarization channels, to insure target visibility, i.e.

$$\begin{aligned} S^{(polinf)}(r) &= (E(\underline{A}^H(r) \underline{X}_{HH,A} \underline{X}_{HH,B}^H \underline{A}(r)) + E(\underline{A}^H(r) \underline{X}_{HV,A} \underline{X}_{HV,B}^H \underline{A}(r)) \\ &\quad + E(\underline{A}^H(r) \underline{X}_{VH,A} \underline{X}_{VH,B}^H \underline{A}(r)) + E(\underline{A}^H(r) \underline{X}_{VV,A} \underline{X}_{VV,B}^H \underline{A}(r))) / 4 \\ &= \underline{A}^H(r) \mathbf{R}_{AB} \underline{A}(r), \end{aligned}$$

where the interferometric correlation matrix is

$$\mathbf{R}_{AB} = \mathbf{R}_{HH,AB} + \mathbf{R}_{HV,AB} + \mathbf{R}_{VH,AB} + \mathbf{R}_{VV,AB}$$

Thus the interferometric MVM and RRMVM images, respectively, are

$$S_{MVM}^{(polinf)}(r) = \frac{\underline{W}^H(r) \mathbf{R}_{avg}^{-1} \mathbf{R}_{AB} \mathbf{R}_{avg}^{-1} \underline{W}(r)}{(\underline{W}^H(r) \mathbf{R}_{avg}^{-1} \underline{W}(r))^2} \quad (46)$$

and

$$S_{RRMVM}^{(polinf)}(r) = \frac{\underline{W}^H(r) (\mu(r) \mathbf{I} + \mathbf{R}_{avg})^{-1} \mathbf{R}_{AB} (\mu(r) \mathbf{I} + \mathbf{R}_{avg})^{-1} \underline{W}(r)}{(\underline{W}^H(r) (\mu(r) \mathbf{I} + \mathbf{R}_{avg})^{-1} \underline{W}(r))^2} \quad (47)$$

Recall that RRMVM exhibits global weak signal suppression in scalar SAR data because of excess degrees of freedom. In an interferometric context, we find that these excess degrees of freedom destroy the interferometric height information, as well. Consequently, we have not found the RRMVM algorithm to be useful in the context of interferometric SAR.

To apply ASR to interferometric data, we again assume balanced and independent thermal noise levels for the two interferometric channels  $A$  and  $B$ , and consequently apply the same processing to channels  $A$  and  $B$ . In this case, the multi-channel ASR algorithm outlined in the previous section employs 16 channels (two I and Q channels for each polarization and interferometric channel). The ASR polarimetric interferogram is simply

$$S_{ASR}^{(polinf)}(r) = (\hat{x}_{HH,A}(r) \hat{x}_{HH,B}^*(r) + \hat{x}_{HV,A}(r) \hat{x}_{HV,B}^*(r) + \hat{x}_{VH,A}(r) \hat{x}_{VH,B}^*(r) + \hat{x}_{VV,A}(r) \hat{x}_{VV,B}^*(r)) / 4. \quad (48)$$

### 3.1 DCS IFSAR Examples

Here we illustrate and compare Fourier, MVM and ASR polarimetric interferograms using X-band data collected of the area around the University of Michigan football stadium by the ERIM-WL DCS IFSAR. The same signal histories, which afford a baseline (Taylor weighted) Fourier image resolution of one meter, were used as input to each of the adaptive imaging algorithms. The rectangularly formatted interferometric signal histories employed were  $600 \times 600$  samples. We computed the Fourier interferogram using Taylor weighting (-35dB peak sidelobe, order 5) to control IPR sidelobes and a zero-pad factor of two. We computed the ASR interferogram using  $M = 4$  (which provides 24 2-D ASR filter taps) and a constraint  $c = 1/4$  from eight sinc IPR Fourier images, each interpolated by a factor of two. We exploited signal history decimation and image mosaicing to compute an MVM interferogram based on 40% subaperture forward-backward averaging. Each decimated signal history aperture was  $50 \times 50$ ; the subaperture size was  $20 \times 20$ . The overall MVM interferogram was computed as a mosaic of  $100 \times 100$  sample overlapping subimages. The final interferogram image sizes for all three methods is  $1200 \times 1200$  samples, of which  $850 \times 1050$  samples are shown.

Figures 18, 19, 20, and 21 illustrate the intensity and phase/height of the Fourier, MVM, SVA, and ASR interferograms, respectively. The relative dB scales for interferogram intensities have been chosen to preserve apparent contrast across the algorithms. Compared against Fourier intensity contrast, MVM loses roughly 10dB of contrast due to the loss of compression gain afforded by the 40% subapertures, SVA contrast is comparable, while ASR improves contrast by roughly 10dB, approximately consistent with theoretical predictions. Qualitatively, the MVM intensity imagery looks more “optical” than the Fourier, displaying both less speckle and sharper resolution of prominent structures. MVM intensity of linear structures is not broken up by IPR scintillation, while the Fourier intensity is. The SVA intensity imagery is somewhat sharper than the Fourier imagery, and comparably speckly. The ASR intensity imagery is specklier and sharper than either the Fourier or SVA imagery. To reduce the phase/height noise of the Fourier and ASR estimates, we applied a  $3 \times 3$  ideal averaging filter to the Fourier, SVA, and ASR interferograms prior to displaying their phases (but not intensities). Without such smoothing, phase/height noise obscures the ASR, and to a lesser extent the SVA and Fourier, height signatures. In contrast, we did not average the MVM interferogram to display its phase; all averaging associated with MVM phase/height estimate occurs in the signal history domain. The principal difference between the Fourier and MVM phase/height imagery is that the Fourier imagery is much noisier, despite filtering. In addition, the MVM phase/height signature displays much sharper definition of the structural detail around the perimeters of the stadium and Crisler arena than the Fourier interferogram. The SVA phase/height imagery offers slightly sharper detail than the Fourier phase/height imagery, as well as slightly less noise. The ASR phase/height imagery has a dramatically different character than that of the Fourier or MVM phase/height imagery. While the ASR height is noisier than the Fourier height, the spatial structures are much better defined in the ASR height image. This is largely due to the fact that the ASR interferogram phase is randomized in the relatively low return areas that surround locally prominent scatterers.

Often, homogeneous SAR clutter intensity is modeled as log-normal. Here we seek to quantify the impact of adaptive imaging on the log (dB) intensity statistics of SAR imagery. Table 4 compares the mean, standard deviation, skewness, and kurtosis of five  $50 \times 50$  sample regions in the Fourier, MVM, SVA, and ASR interferogram dB intensity. The first four regions are spatially homogeneous clutter areas: tree crown, football field, grass, and parking lot; the fifth region is inhomogeneous, containing the building whose ridgelines are clearly visible at the upper right end of the stadium.

Across the clutter regions, the Fourier mean intensity is roughly 6.6dB higher than the mean MVM intensity, suggesting a normalization bias. At the same time, the MVM standard deviation is roughly 2.2dB less than the Fourier standard deviation, reflecting a reduction in speckle across the clutter regions. For the clutter regions, the MVM intensity distribution is less skewed than the Fourier intensity distribution, and also exhibits kurtoses that are closer to three. In general, we conclude that the MVM SAR clutter intensities are better-fit by a log-normal distribution than are the Fourier SAR intensities. Further, the MVM clutter distributions are tighter than the

Statistics of dB intensities, stadium image					
Terrain	Method	mean	std. dev.	skewness	kurtosis
trees	Taylor	187.2	5.09	-.223	3.12
trees	MVM	180.5	3.04	-.174	3.00
trees	SVA	183.7	5.62	-.256	3.08
trees	ASR	174.0	9.26	-.072	2.20
field	Taylor	183.2	3.51	-.529	3.51
field	MVM	176.6	1.24	.072	3.20
field	SVA	179.7	3.93	-.458	3.36
field	ASR	171.2	6.80	-.289	2.44
grass	Taylor	175.4	3.74	-.669	3.86
grass	MVM	169.0	1.48	-.242	2.79
grass	SVA	172.0	4.24	-.579	3.66
grass	ASR	164.5	5.56	-.008	2.74
parking	Taylor	171.7	3.61	-.740	3.72
parking	MVM	165.1	1.41	-.018	2.65
parking	SVA	168.8	3.84	-.608	3.74
parking	ASR	162.8	4.79	-.243	3.01
building	Taylor	185.3	10.56	.504	2.59
building	MVM	177.3	7.38	.391	2.78
building	SVA	182.4	10.54	.474	2.77
building	ASR	170.0	13.55	.846	3.49

Table 4: Statistics of polarimetric interferometric dB intensities over homogeneous clutter areas and building structure.

corresponding Fourier distributions, yet equally well separated. On the building, the Fourier mean intensity is 8.0dB higher than the mean MVM intensity, a differential that is 1.4dB higher (worse for MVM) than in clutter. The MVM standard deviation is roughly 3.2dB less than the Fourier standard deviation over the building, the MVM intensity is less skewed than the Fourier imagery, and exhibits higher kurtosis, as well. The fact that the MVM image displays greater kurtosis yet smaller standard deviation than the Fourier image on the building structure suggests that MVM does a better job of separating the prominent scatterers on the building's roof from the surrounding scattering structures.

Across the clutter regions, the Fourier mean intensity is roughly 3.2dB higher than the mean SVA intensity, again suggesting a normalization bias. The standard deviation of the SVA intensity is roughly .4dB higher than the Fourier standard deviation. The skewness and kurtosis of the SVA and Fourier intensity is comparable. Thus the statistics of the SVA intensity are essentially the same as those of Fourier intensity.

Since we employed an underdetermined ASR filter (24 degrees of freedom, 8 I/Q channels), there was a risk that some of the ASR interferogram intensities would be zero, causing the statistics of the dB intensities to be undefined. While this did not occur, the underdetermined ASR filter does impact the dB intensity distribution in two undesirable ways. First, the ASR mean intensity is less than the Fourier mean intensity by between roughly

9dB and 15dB, where the differential is larger for strong return areas than for weak return areas. Second, the ASR standard deviation is much larger than the Fourier standard deviation, reflecting the fact that underdetermined ASR exacerbates speckle. Together, these factors may diminish the differentiability of natural and man-made objects in the ASR scene. For example, the Fourier mean intensity differential between building and field is 2.1dB, the ASR differential is -1.2dB, a loss of 3.3dB in contrast. At the same time, the standard deviation of the ASR intensities for the tree and building areas is roughly 3.6dB greater than with Fourier. On the other hand, if we evaluate the mean values of the interferogram intensity, rather than the dB intensity, and compare the ratio of building mean intensity to field mean intensity, then ASR provides a contrast improvement of 3.0dB over Fourier; this is the sense in which our TCR analysis suggests that ASR improves contrast.

To compare the interferometric height accuracy of the methods, we evaluated the mean and standard deviation of the polarimetric interferogram phase over four flat regions ( $30 \times 30$  pixels) within the stadium scene: a roof, the football field, two other grassy regions, a low-return parking lot (which we expect to be noisy). Table 5 compares these statistics for Fourier, MVM, SVA, and ASR imagery, with and without interferogram averaging by an ideal  $3 \times 3$  smoothing kernel.

Statistics interferometric phase, stadium image									
Region	Statistic	Taylor	MVM	SVA	ASR	Taylor $3 \times 3$ LPF	MVM $3 \times 3$ LPF	SVA $3 \times 3$ LPF	ASR $3 \times 3$ LPF
roof	mean	-3.28	-3.77	-3.64	-4.26	-3.61	-3.80	-3.84	-3.57
roof	stddev	11.70	4.05	15.76	74.33	7.92	3.73	6.47	18.82
field	mean	10.24	10.03	10.04	4.30	10.17	10.02	10.05	9.82
field	stddev	8.84	2.83	14.88	54.47	5.25	2.56	5.13	9.82
grass 1	mean	7.83	7.56	8.74	9.68	7.31	7.54	8.10	10.72
grass 1	stddev	12.97	3.63	17.85	58.70	6.93	3.18	6.47	15.39
grass 2	mean	2.90	3.15	3.69	2.24	2.90	3.20	3.38	5.15
grass 2	stddev	18.58	5.35	26.46	71.79	10.42	4.86	9.22	27.83
parking lot	mean	0.38	2.04	1.52	4.42	2.01	1.97	1.27	3.34
parking lot	stddev	33.59	7.13	41.01	83.19	17.26	6.23	15.11	44.87

Table 5: Statistics of polarimetric interferometric phase over homogeneous level areas.

With the exception of the low-return parking lot, there is generally good agreement (less than  $1.4^\circ$  difference) between the unfiltered and filtered Fourier, SVA and MVM mean phases. Also, filtering has relatively little impact on the Fourier, SVA, and MVM mean phases. While filtering reduces the standard deviation of the Fourier phases by a factor of 1.7, it reduces the standard deviations of the MVM phases by only a factor of 1.1; filtering reduces the standard deviation of the SVA phases by a large factor of 2.8. The unfiltered Fourier phase standard deviations are roughly 3.0 times as large as those of the unfiltered MVM phase standard deviations. The *filtered* Fourier phase standard deviations remain roughly 1.9 times as large as those of the *unfiltered* MVM phase standard deviations.

Although the unfiltered SVA phase standard deviations are significantly larger than the unfiltered Fourier standard deviations, the filtered SVA phase standard deviations are smaller than the filtered Fourier standard deviations. The Fourier, SVA, and MVM interferogram phases are equally accurate, yet the MVM phases are both less noisy and resolve finer structural detail; if spatial averaging is performed, the SVA phases are also less noisy and sharper than the corresponding Fourier phases.

In contrast, the unfiltered ASR mean phases can be as much as  $6.0^\circ$  different from the unfiltered Fourier mean phases, and display huge standard deviations. However, filtering the ASR interferogram improves its phase enormously, reducing its phase standard deviations by roughly a factor of 3.6 and causing its mean phase to be less than  $3.5^\circ$  from the filtered Fourier mean phase. The reason that filtering the interferograms has a relatively greater impact on underdetermined ASR phase than Fourier or MVM phase is that many of the ASR pixels display very low intensity. The phase of the low intensity pixels is effectively garbage, which manifests itself as the huge phase standard deviation. However, the phase accuracy of the prominent points is relatively good (comparable to the Fourier). Since the interferogram effectively weights each pixel by its intensity, spatial smoothing of the interferogram spreads the phases of the good pixels spatially, replacing the phase of the bad pixels.

## 4 Conclusions

This paper discussed the rationale for using modern 2-D spectral estimation algorithms, rather than Fourier transforms, to form SAR imagery, and provided numerous examples of their application to collected SAR data. Of the methods discussed here, the adaptive methods that seem to offer the most immediate utility are MVM, Pisarenko, ASR and SVA. MVM and Pisarenko offer improved resolution of prominent scatterers, reduced speckle, and imagery that is more "optical" in character than Fourier imagery. Pisarenko's method produces cleaner imagery than conventional ARLP, and obviates the need to choose a prediction element, since Pisarenko averages over all ARLP prediction elements. SVA offers sinc-like resolution without sidelobe artifacts; ASR offers slightly sharper resolution as well as TCR gain, albeit at the cost of increased speckle. The computational burden of SVA and ASR is trivial compared with that of MVM and Pisarenko. EV offers great potential for enhancing resolution and contrast in SAR imagery; however, sophisticated new methods for estimating model order, based on spatial content, rather than simply intensity, must be developed before EV can realize its full potential. Methods such as PML and TKARLP offer great promise for specialized applications in which accurate localization of point scatterers is of paramount importance, but offer little utility for general SAR imaging.

We showed how MVM, ASR and SVA methods can be extended to estimate height interferometrically, and demonstrated that these methods offer significant improvement over Fourier methods for imaging interferometric scattering intensity and height. MVM simultaneously improves resolution and reduces the noise of both intensity

and height imagery. Over homogeneous regions, MVM intensity is distributed more log-normally than corresponding Fourier intensity. ASR improves the spatial definition one sees in interferometric height signatures, although it also increases noise. SVA both improves spatial definition of and reduces noise of interferometric height signatures slightly.

The ultimate utility of these adaptive imaging algorithms for various SAR applications has yet to be established. For example, it is unclear whether and/or to what degree these methods will improve automatic target detection and recognition performance. Similarly, the ramifications of these methods for systems-related issues such as area coverage rate, and requirements on motion compensation accuracy have yet to be addressed. Many other questions exist, as well. Which methods are most appealing to SAR image analysts? Which methods produce imagery that is best suited to subsequent enhancement, exploitation, or compression methods? Is the computational burden imposed by MVM, Pisarenko, and EV prohibitive, or just large? This paper has demonstrated that the impact these adaptive algorithms have on SAR imagery can be dramatic, and that there is reason to believe that imaging techniques based on modern 2-D spectral estimation methods may prove valuable in the SAR community.

## 5 Acknowledgements

This work was supported by the Advanced Research Projects Agency (DoD), Advanced Systems Technology Office, under contract DAAH01-93-C-R178. Approved for public release; distribution unlimited. The author wishes to thank Wright Laboratory for providing DCS SAR data of the ships near Toledo, OH, and DCS fully polarimetric IFSAR data of the area around the University of Michigan football stadium.

## References

- [1] J. Walker, "Range-Doppler imaging of rotating objects," *IEEE Trans. Aerosp., Elec. Sys.*, vol. AES-16, no. 1, 1980.
- [2] M. Soumekh, "A System Model and Inversion for Synthetic Aperture Radar Imaging," *IEEE Trans. on Image Proc.*, vol. 1, no. 1, 1992.
- [3] S. M. Kay, *Modern Spectral Estimation Theory and Application*, Prentice-Hall, Englewood Cliffs, 1988.
- [4] S. L. Marple, Jr., *Digital Spectral Analysis with Applications*, Prentice-Hall, Englewood Cliffs, 1987.
- [5] S. M. Kay, S. L. Marple, "Spectrum Analysis — A Modern Perspective," *Proc. IEEE*, vol. 69, Nov. 1981.
- [6] D. H. Johnson, "The Application of Spectral Estimation Methods to Bearing Estimation Problems," *Proc. IEEE*, vol. 70, no. 9, Sep. 1982.
- [7] J. P. Burg, "Maximum Entropy Spectral Analysis," Ph.D. dissertation, Dep. Geophys., Stanford Univ., Stanford, CA, 1967.
- [8] R. T. Lacoss, "Data Adaptive Spectral Analysis Methods," *Geophys.*, vol. 36, Aug. 1971.
- [9] V. F. Pisarenko, "On Estimation of Spectra by Means of Nonlinear Function of the Covariance Matrix," *Geophys. J. Roy. Astron. Soc.*, vol. 28, 1972, pp. 511-531.
- [10] W. F. Gabriel, "Spectral Analysis and Adaptive Array Superresolution Techniques," *Proc. IEEE*, vol. 68, Jun. 1980.
- [11] L. Marple, "A New Autoregressive Spectrum Analysis Algorithm," *IEEE Trans. Acoust., Speech, Sig. Proc.*, vol. ASSP-28, Aug. 1980.
- [12] S. R. DeGraaf, D. H. Johnson, "Capability of Array Processing Algorithms to Estimate Source Bearings," *IEEE Trans. Acoust., Speech, Sig. Proc.*, vol. ASSP-33, no. 6, Dec. 1985.
- [13] R. Schmidt, "Multiple Emitter Location and Signal Parameter Estimation," *Proc. RADC Spec. Est. Workshop*, 1979.
- [14] D. H. Johnson, S. DeGraaf, "Improving the Resolution of Bearing in Passive Sonar Arrays by Eigenvalue Analysis," *IEEE Trans. Acoust., Speech, Sig. Proc.*, vol. ASSP-30, no. 4, Aug. 1982.
- [15] D. Tufts, R. Kumaresan, "Frequency Estimation of Multiple Sinusoids: Making Linear Prediction Perform Like Maximum Likelihood," *Proc. IEEE*, vol. 70, Sep. 1982.
- [16] A. J. Barabell, "Improving the Resolution Performance of Eigenstructure-Based Direction-Finding Algorithms," *Proc. ICASSP*, 1983.
- [17] S. R. DeGraaf, "Parametric Estimation of Complex 2-D Sinusoids," *IEEE Fourth Annual ASSP Workshop on Spectrum Estimation and Modeling*, Aug. 1988.
- [18] P. Stoica, A. Nehorai, "MUSIC, Maximum Likelihood, and Cramer-Rao Bound," *IEEE Trans. Acoust., Speech, Sig. Proc.*, vol. 37, no. 5, May 1989.
- [19] R. Roy, T. Kailath, "ESPRIT — Estimation of Signal Parameters via Rotational Invariance Techniques," *IEEE Trans. Acoust., Speech, Sig. Proc.*, vol. 37, no. 7, Jul. 1989.



- [20] B. D. Rao, K. V. S. Hari, "Performance Analysis of Root-MUSIC," *IEEE Trans. Acoust., Speech, Sig. Proc.*, vol. 37, no. 12, Dec. 1989.
- [21] P. Stoica, K. C. Sharman, "Maximum Likelihood Methods for Direction-of-Arrival Estimation," *IEEE Trans. Acoust., Speech, Sig. Proc.*, vol. 38, no. 7, Jul. 1990.
- [22] M. I. Miller, D. R. Fuhrmann, "Maximum-Likelihood Narrow-Band Direction Finding and the EM Algorithm," *IEEE Trans. Acoust., Speech, Sig. Proc.*, vol. 38, no. 9, Sep. 1990.
- [23] B. Armour, S. D. Morgera, "Exact Forward-Backward ML AR Parameter Estimation Method," *IEEE Trans. Acoust., Speech, Sig. Proc.*, vol. 39, no. 9, Sep. 1991.
- [24] A. L. Swindlehurst, B. Ottersten, R. Roy, T. Kailath, "Multiple Invariance ESPRIT," *IEEE Trans. Acoust., Speech, Sig. Proc.*, vol. 40, no. 4, Apr. 1992.
- [25] D. Storer, A. Nehorai, "Newton Algorithms for Conditional and Unconditional Maximum Likelihood Estimation of the Parameters of Exponential Signals in Noise," *IEEE Trans. Acoust., Speech, Sig. Proc.*, vol. 40, no. 6, Jun. 1992.
- [26] L. B. Jackson, H. C. Chien, "Frequency and Bearing Estimation by Two-Dimensional Linear Prediction," *Proc. ICASSP'79*, Apr. 1979.
- [27] J. S. Lim, N. A. Malik, "A New Algorithm for Two-Dimensional Maximum Entropy Power Spectrum Estimation," *IEEE Trans. Acoust., Speech, Sig. Proc.*, vol. ASSP-29, Jun. 1981.
- [28] R. Kumaresan, D. W. Tufts, "A Two-Dimensional Technique for Frequency-Wavenumber Estimation," *Proc. IEEE*, vol. 69, Nov. 1981.
- [29] J. H. McClellan, "Multidimensional Spectral Estimation," *Proc. IEEE*, vol. 70, Sep. 1982.
- [30] N. A. Malik, J. S. Lim, "Properties of Two-Dimensional Maximum Entropy Power Spectrum Estimates," *IEEE Trans. Acoust., Speech, Sig. Proc.*, vol. ASSP-30, Oct. 1982.
- [31] B. F. McGuffin, B. Liu, "An Efficient Algorithm for Two-Dimensional Autoregressive Spectrum Estimation," *IEEE Trans. Acoust., Speech, Sig. Proc.*, vol. 37, no. 1, Jan. 1989.
- [32] I. J. Gupta, "Performance of Super Resolution Techniques in Imaging Compact Ranges Probe Data," *Proc. AMTA Symposium, Boulder, CO*, Oct. 1991.
- [33] E. K. Walton, "Superresolution Radar Target Imaging," *Proc. AMTA Symposium, Boulder, CO*, Oct. 1991.
- [34] M. M. Giray, "Super-resolution Techniques in RCS Signature Analysis," *Proc. AMTA Symposium, Boulder, CO*, Oct. 1991.
- [35] B. W. Deats, D. J. Farina, "Superresolution Signal Processing for RCS Measurement Analysis," *Proc. AMTA Symposium, Boulder, CO*, Oct. 1991.
- [36] A. Bati, D. Mensa, K. Vaccaro, "Applicability of Maximum Entropy Methods to RCS Analysis," *Proc. AMTA Symposium, Columbus, OH*, Oct. 1992.
- [37] M. M. Giray, S. R. Mishra, "A Comparative Study of MUSIC and ESPRIT Methods in Scattering Analysis," *Proc. AMTA Symposium, Columbus, OH*, Oct. 1992.

- [38] E. K. Walton, I. J. Gupta, M. W. Tu, A. Moghaddar, "Super Resolution Radar Target Imaging of Realistic Targets," Proc. AMTA Symposium, Columbus, OH, Oct. 1992.
- [39] A. Moghaddar, I. J. Gupta, "High Resolution Radar Imagery Using Parametric Modeling and Data Extrapolation," Proc. AMTA Symposium, Columbus, OH, Oct. 1992.
- [40] Y. Hua, F. Baqai, Y. Zhu, D. Heilbronn, "Imaging of Point Scatterers from Step-Frequency ISAR Data," Proc. AMTA Symposium, Columbus, OH, Oct. 1992.
- [41] E. C. Burt, T. G. Moore, B. Zuerndorfer, "Range Resolution Enhancement for Identification," *1992 Joint Service Combat Identification Systems Conference Technical Proceedings*, Laurel, MD, Jul. 1992.
- [42] S. D. Cabrera, B. C. Flores, G. Thomas, J. Vega-Pineda, "Evolutionary Spectral Estimation Based on Adaptive Use of Weighted Norms," Proc. 1994 SPIE Workshop, Algorithms for Synthetic Aperture Radar, Orlando, FL, May 1994.
- [43] G. R. Benitz, "Preliminary Results in Adaptive High Definition Imaging for Stationary Targets," *MIT Lincoln Laboratory Project Report AST-34*, Nov. 1993.
- [44] S. R. DeGraaf, "Sidelobe Reduction via Adaptive FIR Filtering in SAR Imagery," *IEEE Trans. on Image Proc.*, vol. 3, no. 3, May 1994.
- [45] S. R. DeGraaf, "SAR Imaging via Modern 2-D Spectral Estimation Methods," Proc. 1994 SPIE Workshop, Algorithms for Synthetic Aperture Radar, Orlando, FL, May 1994.
- [46] J. W. Odendaal, E. Barnard, C. W. I. Pistorius, "Two-Dimensional Superresolution Radar Imaging Using the MUSIC Algorithm," *IEEE Trans. Ant. Prop.*, vol. 42, no. 10, Oct. 1994.
- [47] H. C. Stankwitz, R. J. Dallaire, J. R. Fienup, "Non-linear Apodization for Sidelobe Control in SAR Imagery," *IEEE Trans. Aerosp., Elec. Sys.*, vol. 31, no. 1, Jan. 1995.

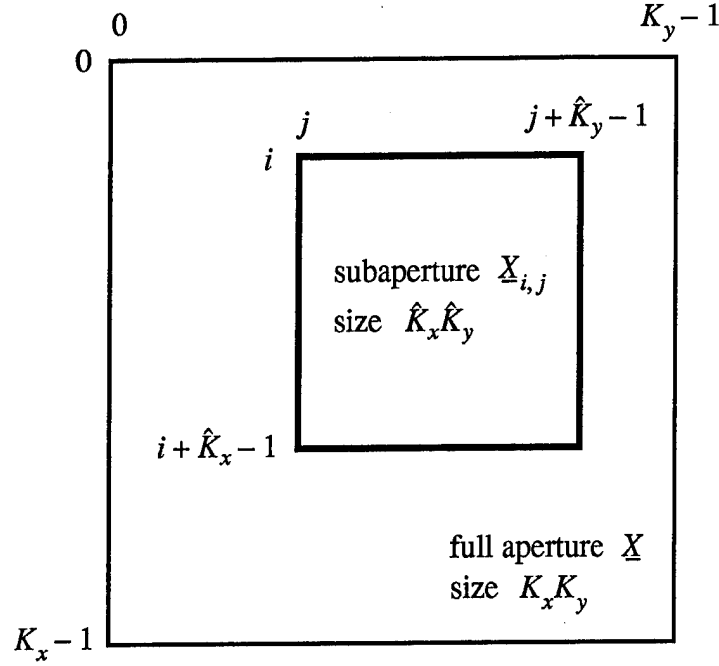


Figure 1: Extraction of a single signal history subaperture from within the full (decimated) aperture.

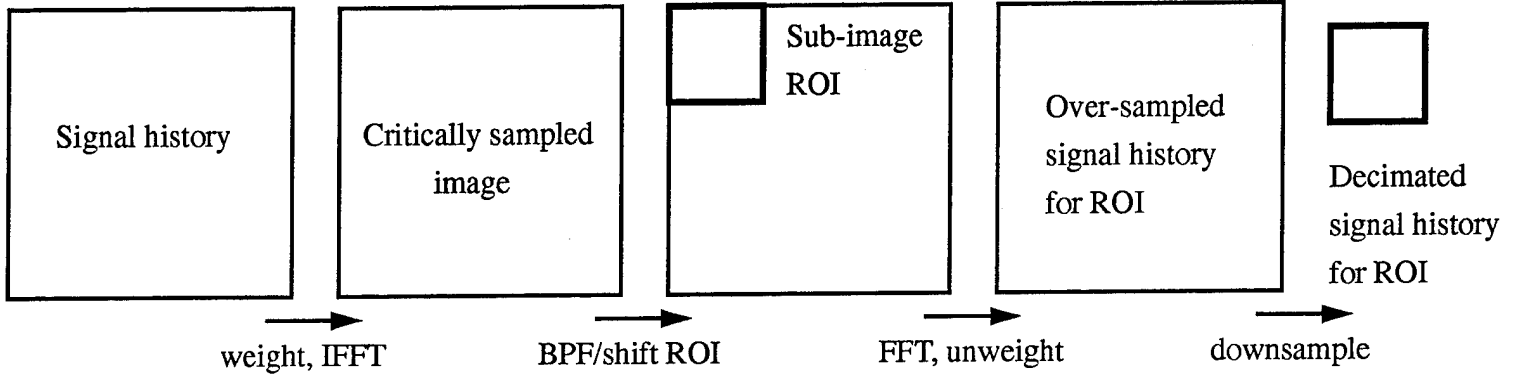


Figure 2: Decimation of signal history to represent a sub-image region of interest.

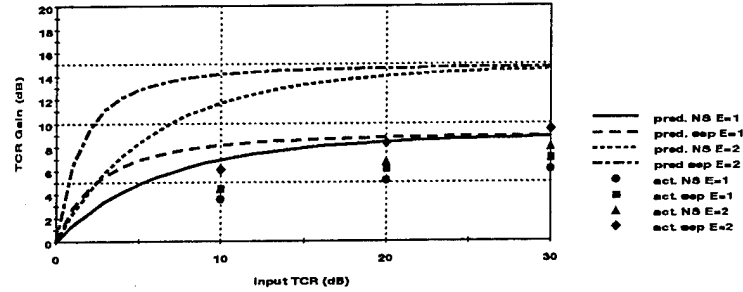


Figure 3: Comparison of theoretically predicted and observed TCR gain provided by the ASR algorithm as a function of input TCR for nonseparable and separable filters using constraints satisfying

$$\varepsilon = \mathcal{M}c^2 = 1, 2$$

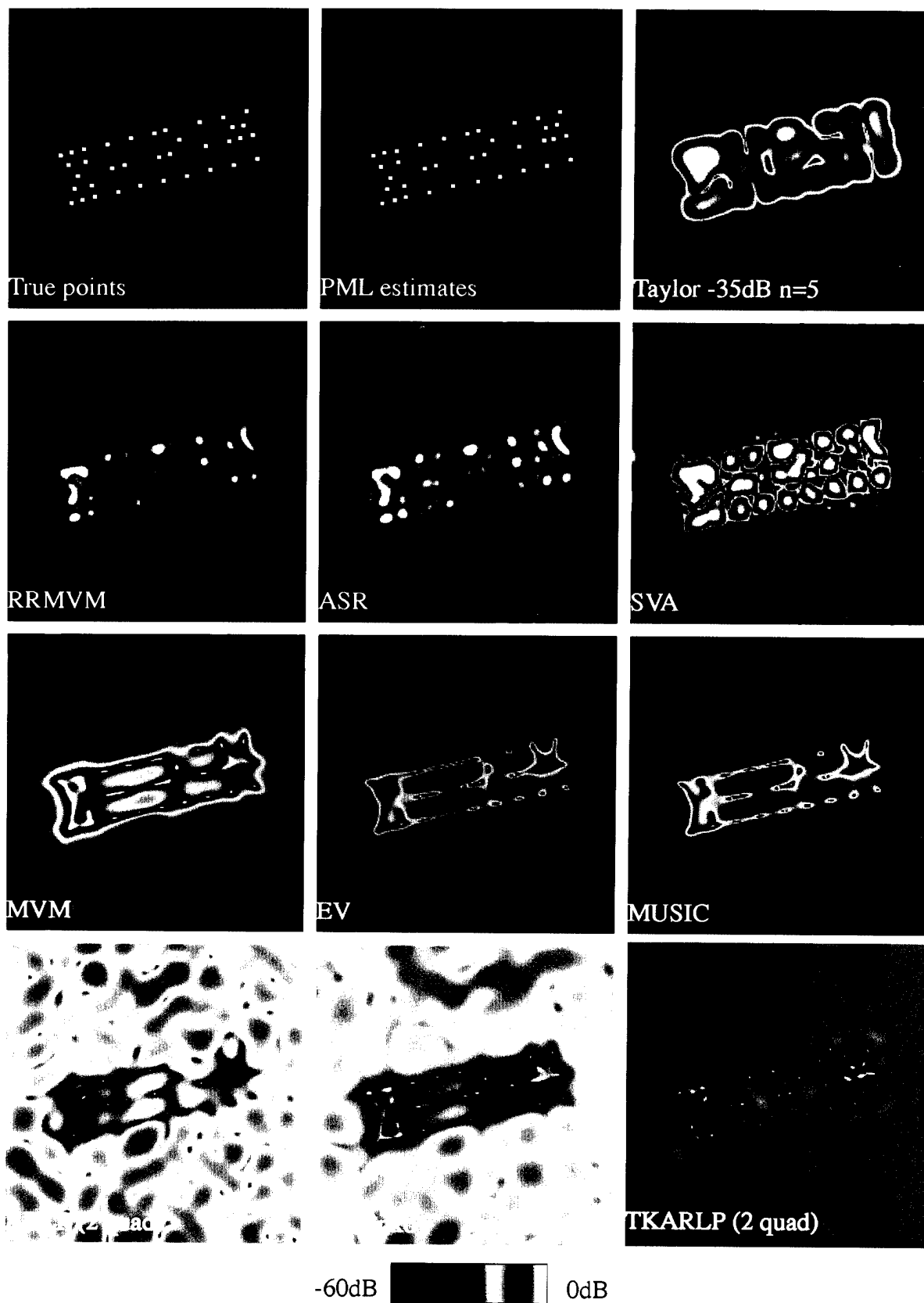


Figure 4: Comparison of 2-D spectral estimation techniques for imaging synthetic point scatterers. Image-domain TCR is 33dB.

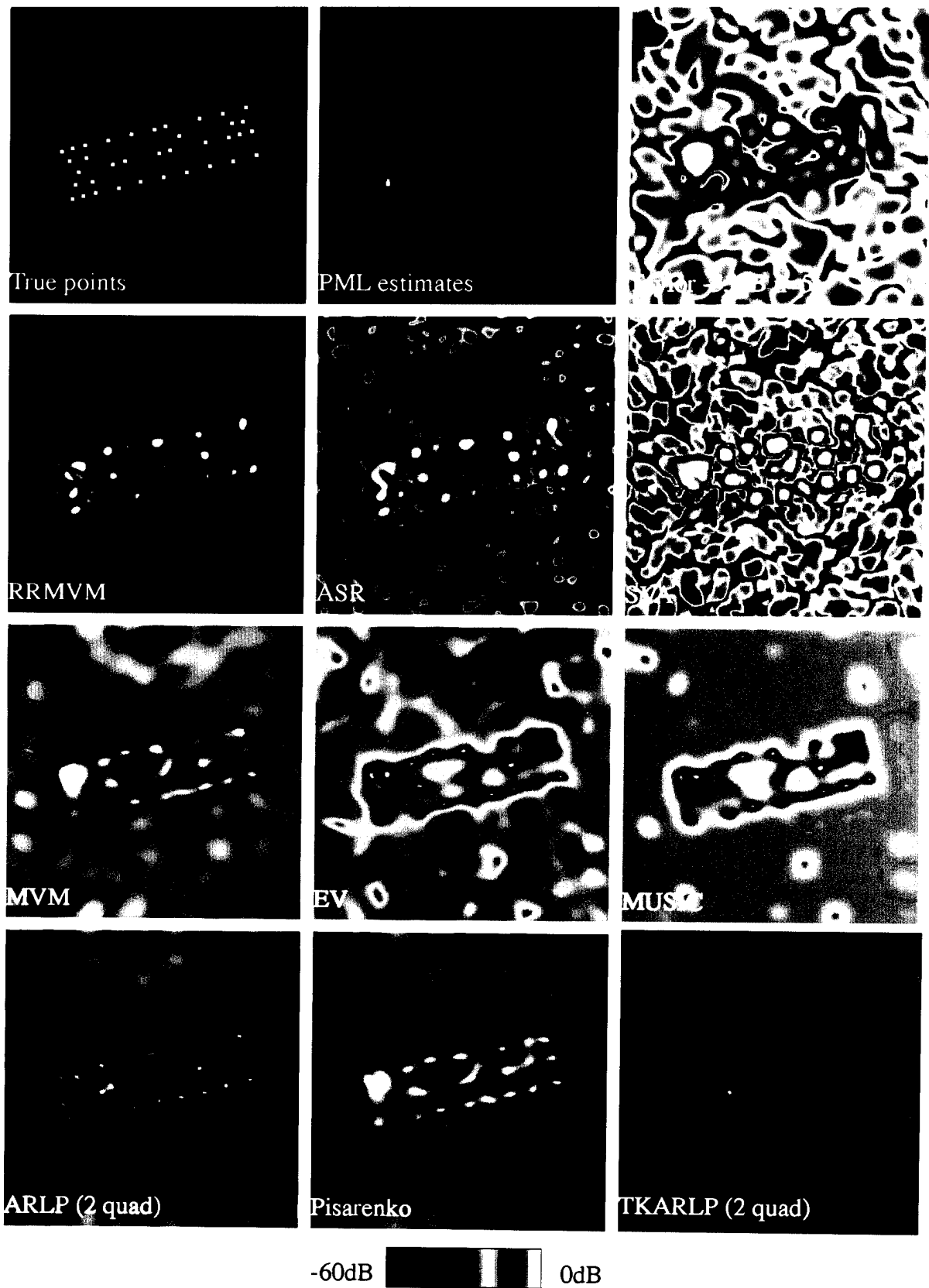


Figure 5: Comparison of 2-D spectral estimation techniques for imaging synthetic point scatterers. Image-domain TCR is 13dB.

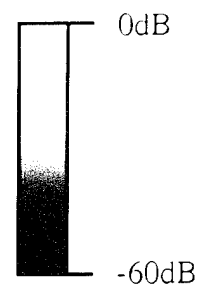
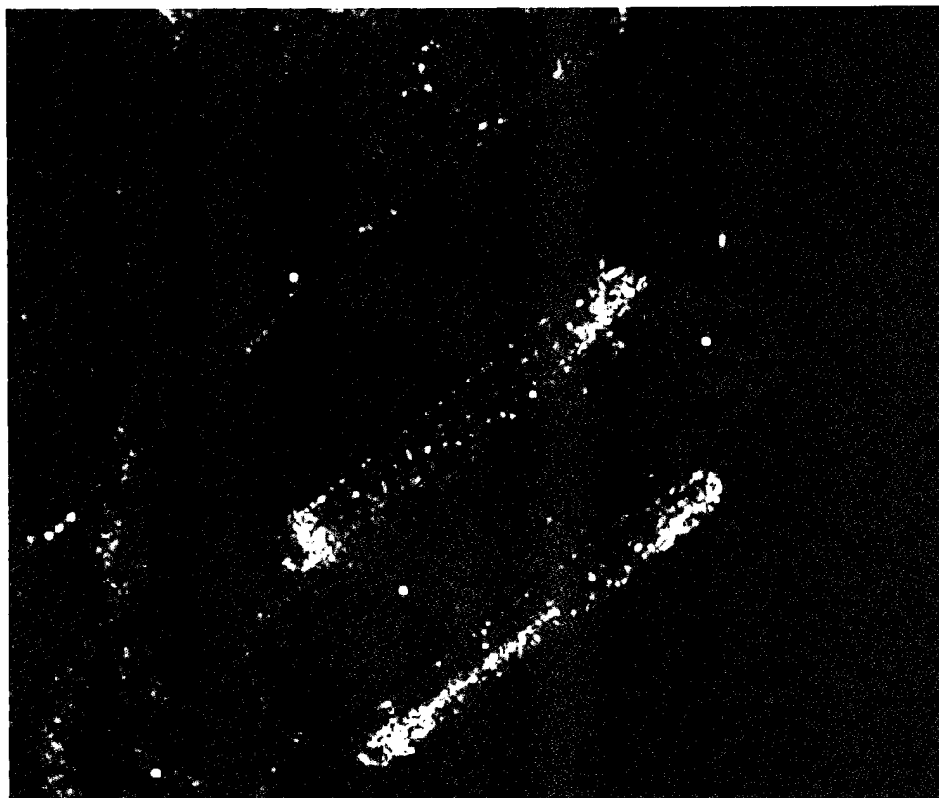


Figure 6: Baseline Taylor-weighted (-35dB,  $n=5$ ) Fourier imagery.

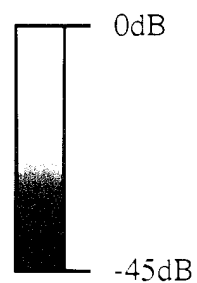
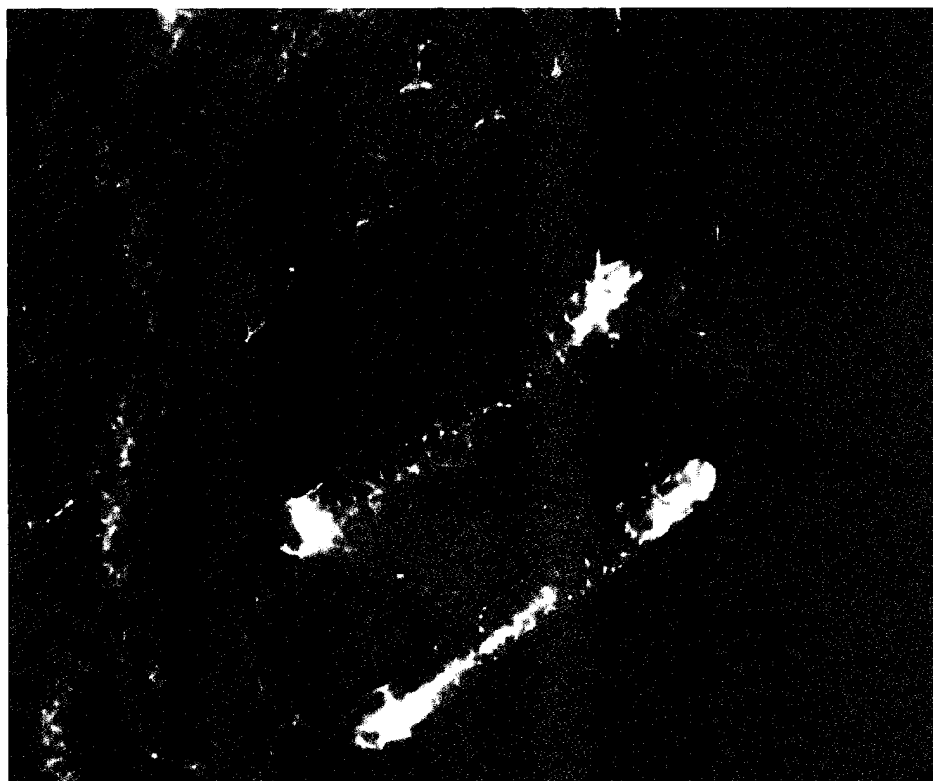


Figure 7: 40% subaperture MVM imagery.

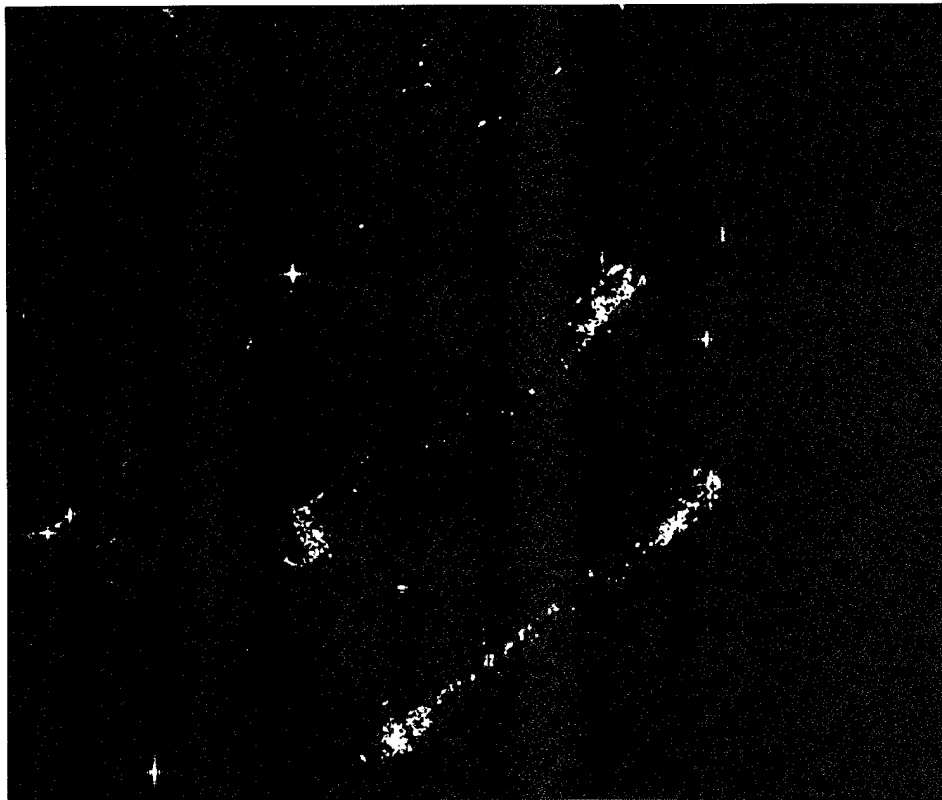


Figure 8: 400/402 subaperture RRMVM ( $c=1.002$ ) imagery.



Figure 9: ASR (order=2,  $c=.5$ ) imagery.

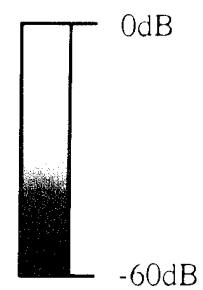
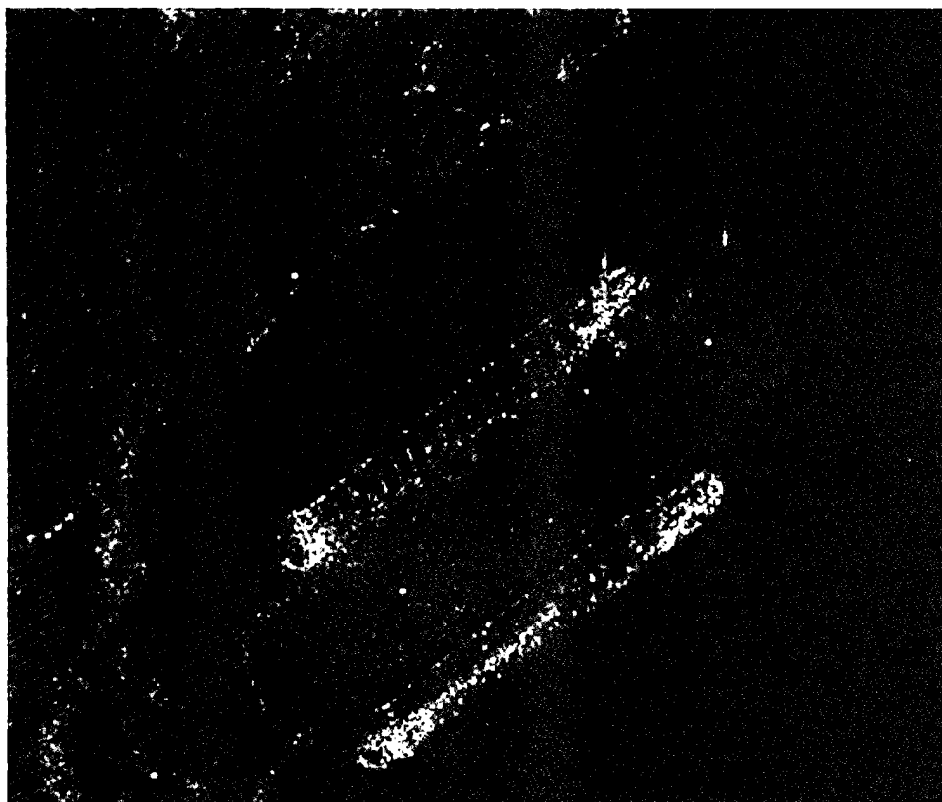


Figure 10: SVA imagery.

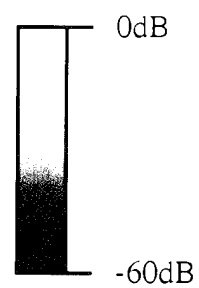
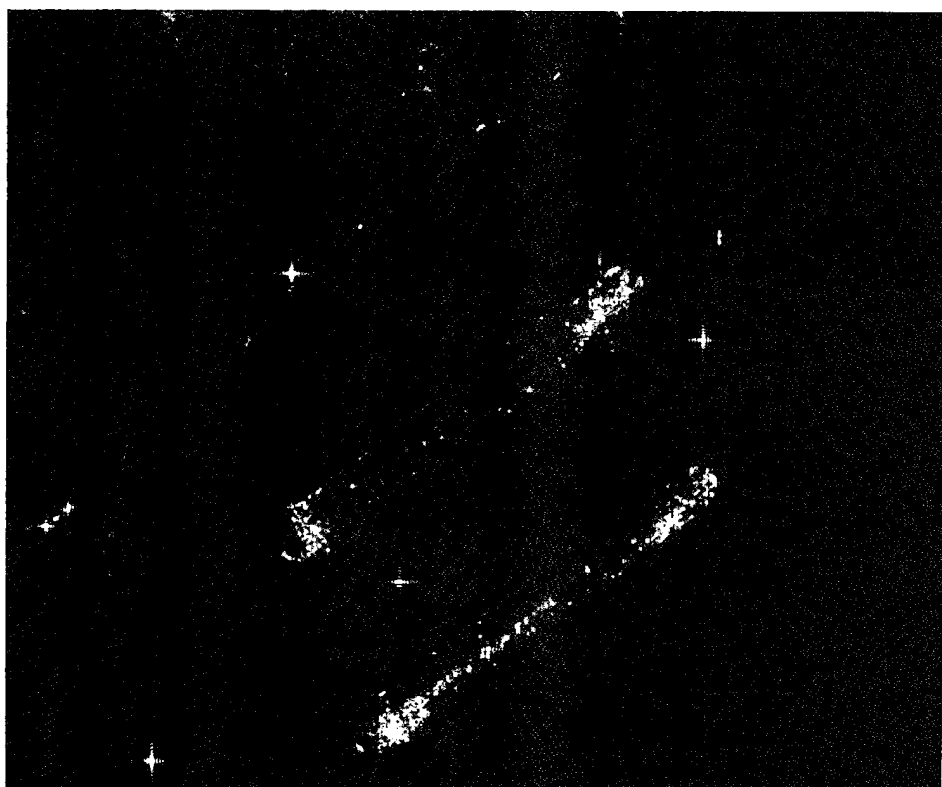


Figure 11: Unweighted (sinc IPR) Fourier imagery.



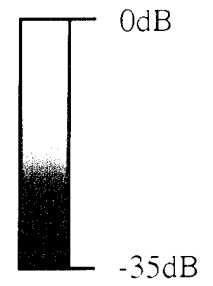
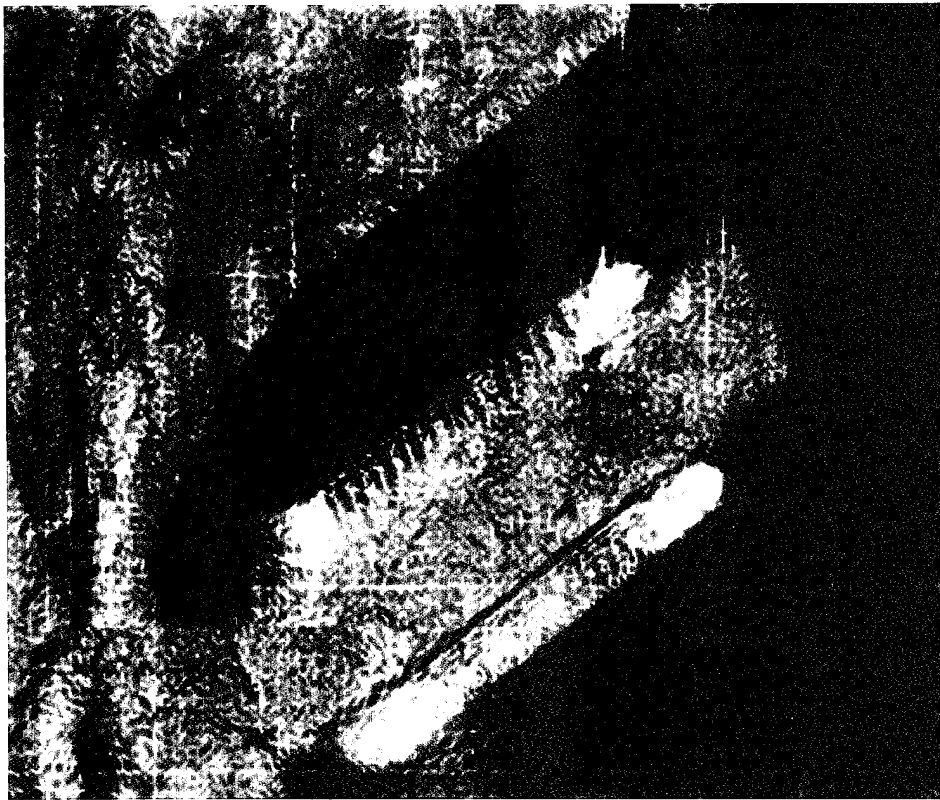


Figure 12: 40% subaperture ARLP (first- and second-quad. avg.) imagery.

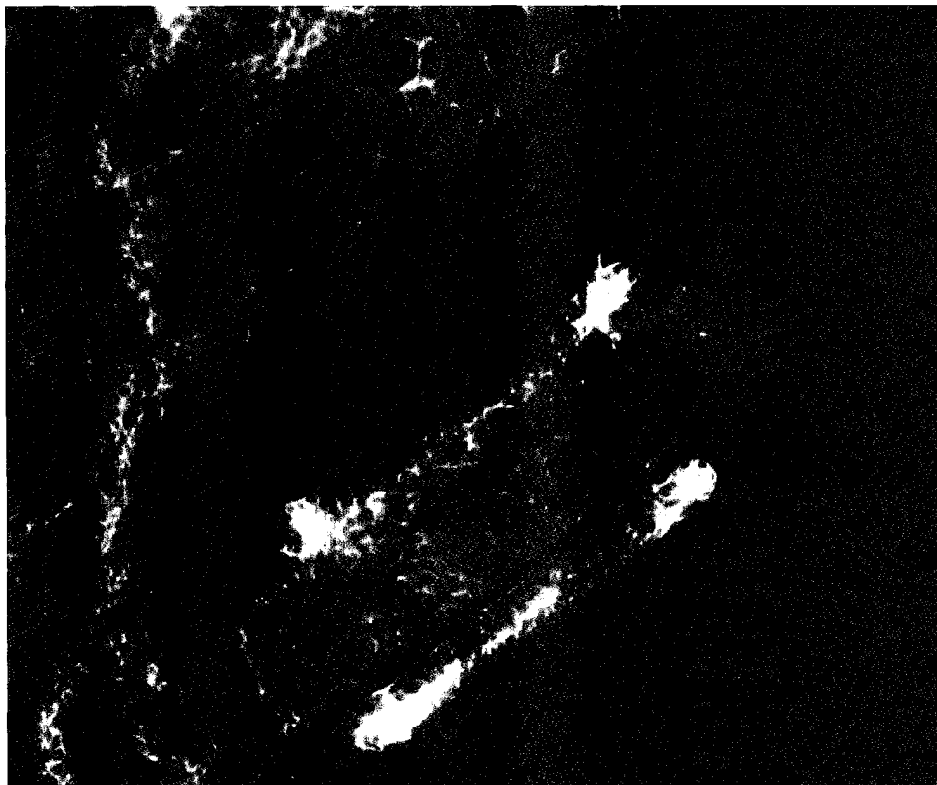


Figure 13: 40% subaperture Pisarenko imagery.

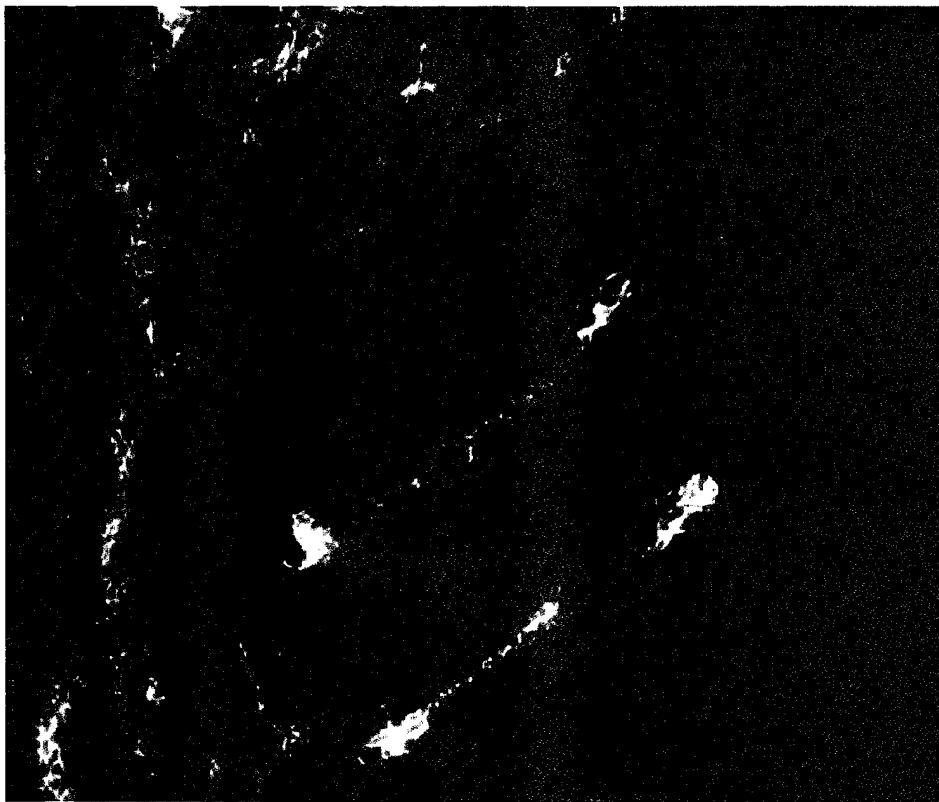


Figure 14: 40% subaperture EV imagery (90% energy order criterion).

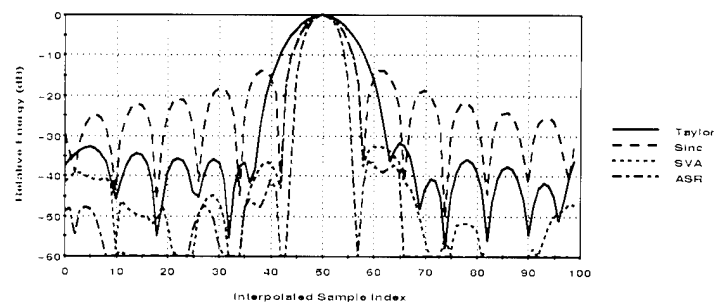


Figure 15: Interpolated slices through trihedral on causeway, "easy" methods.

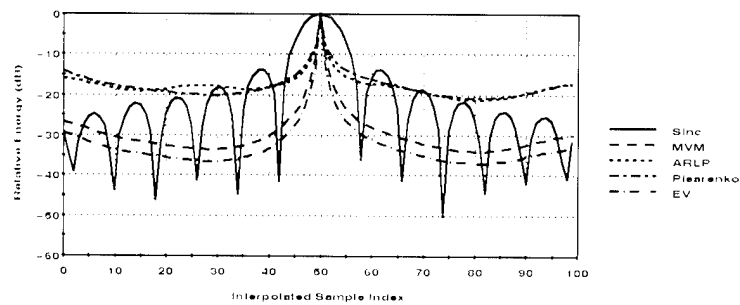
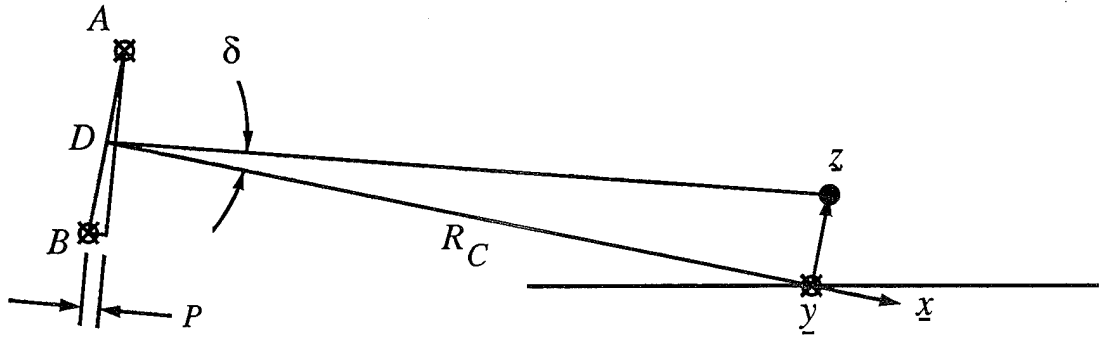


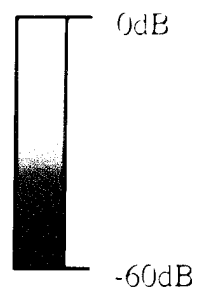
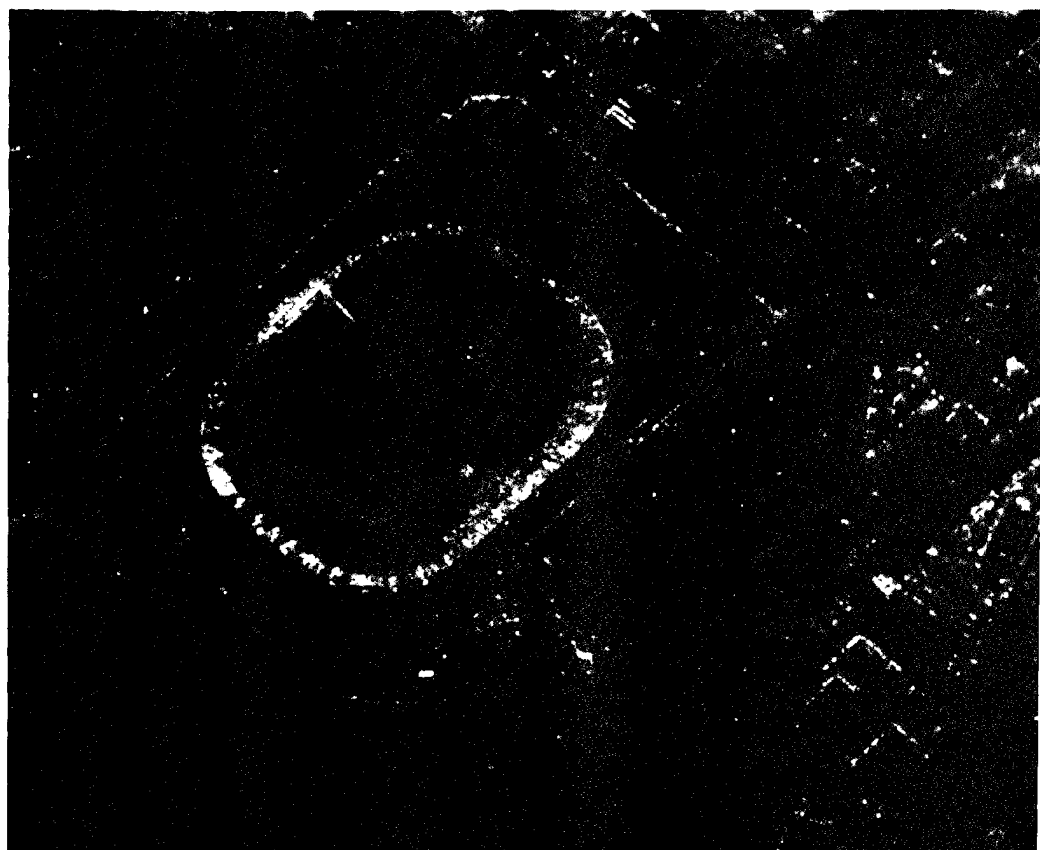
Figure 16: Interpolated slices through trihedral on causeway, "hard" methods.



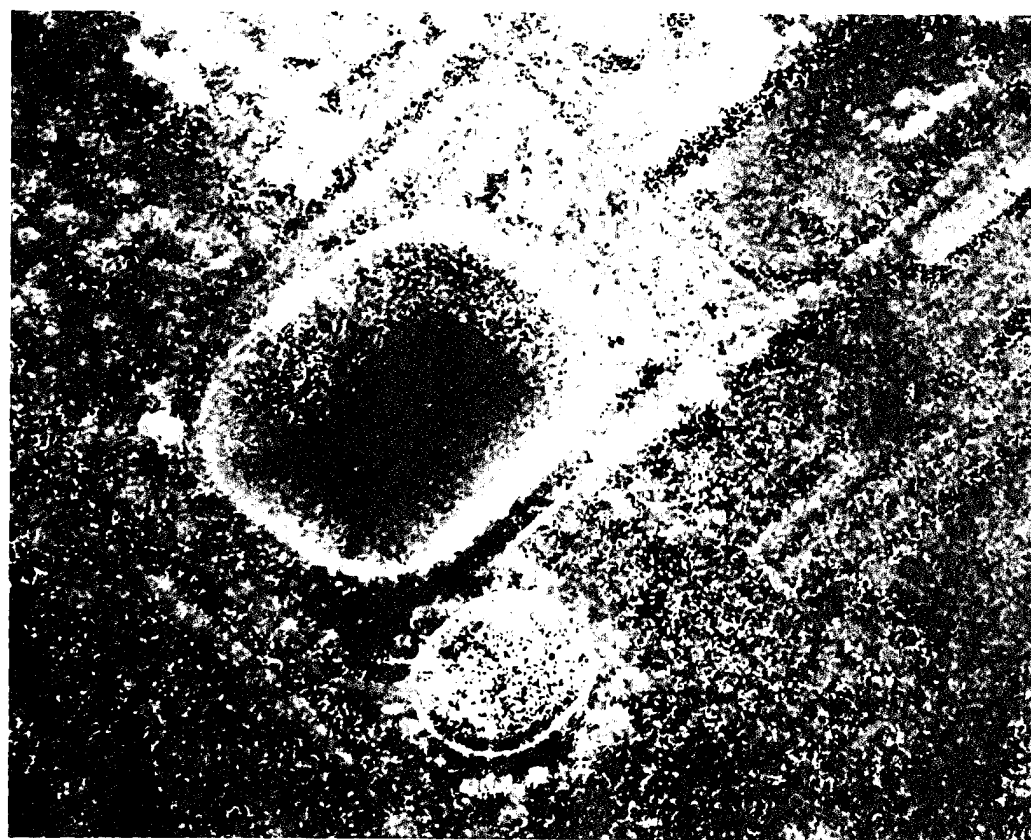
Plane-wave path length difference  $P$  satisfies  $\frac{P}{D} \approx \tan \delta = \frac{z}{R_C + x} \approx \frac{z}{R_C}$

Image phase difference is  $\phi = \angle(AB^*) = \frac{P}{\lambda_C} = \frac{D}{R_C \lambda_C} z$

Figure 17: Geometric and conceptual foundation of interferometric SAR imaging.

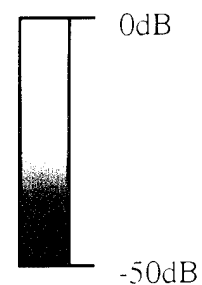
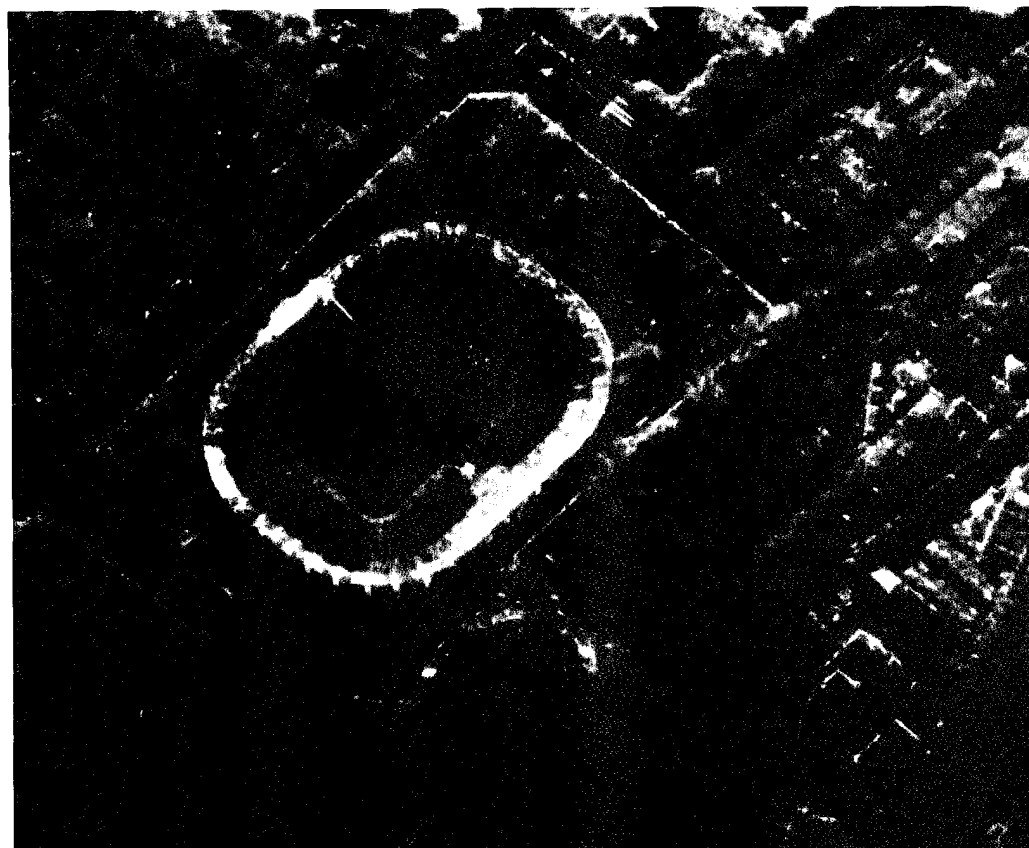


relative  
intensity

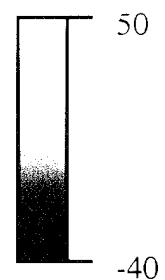
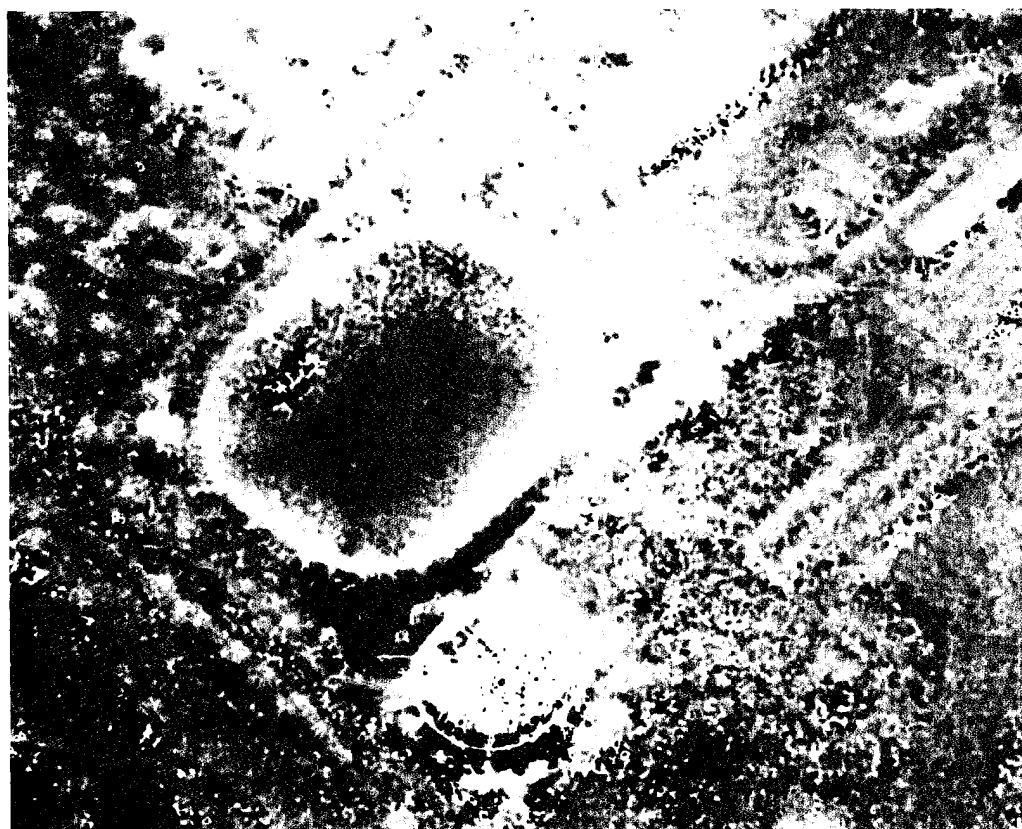


interferometric  
phase (deg)  
3X3 ideal LPF

Figure 18: Baseline Taylor-weighted (-35dB,  $n=5$ ) Fourier interferogram.

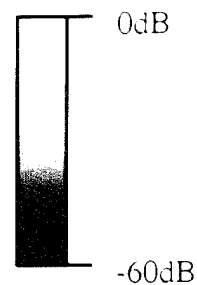
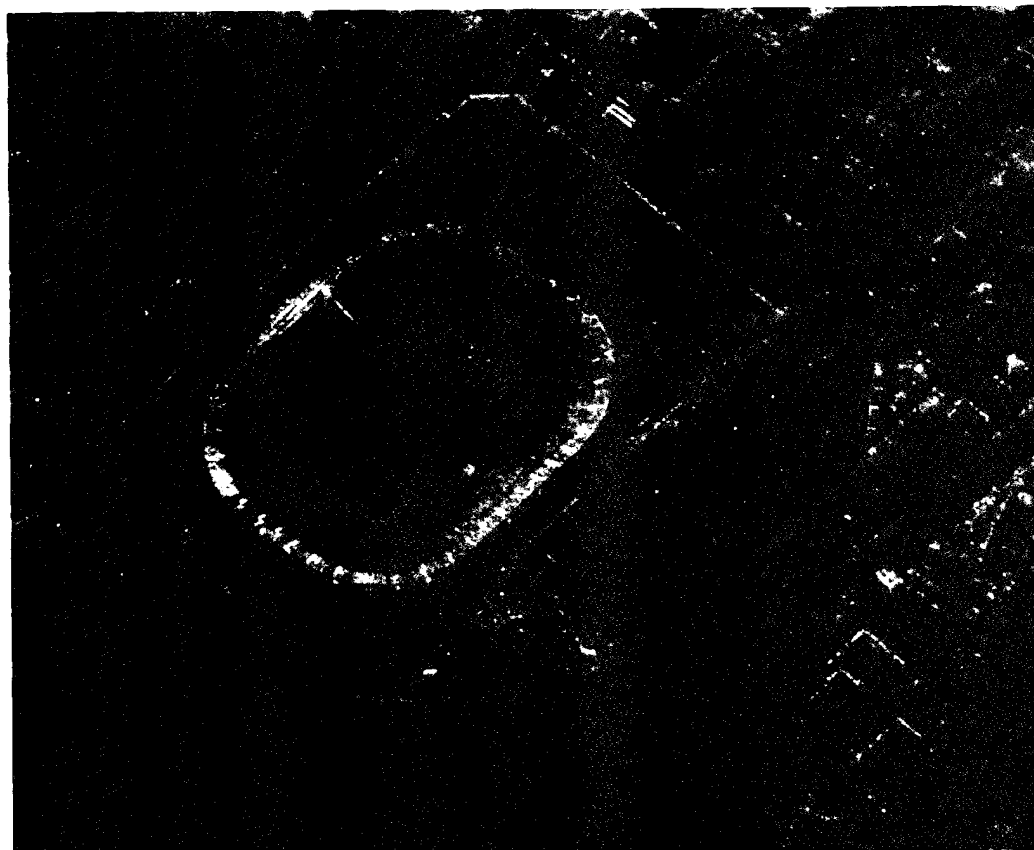


relative  
intensity



interferometric  
phase (deg)

Figure 19: 40% subaperture MVM interferogram.

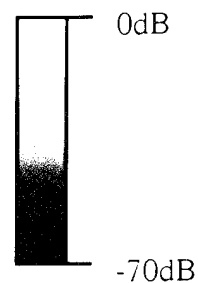
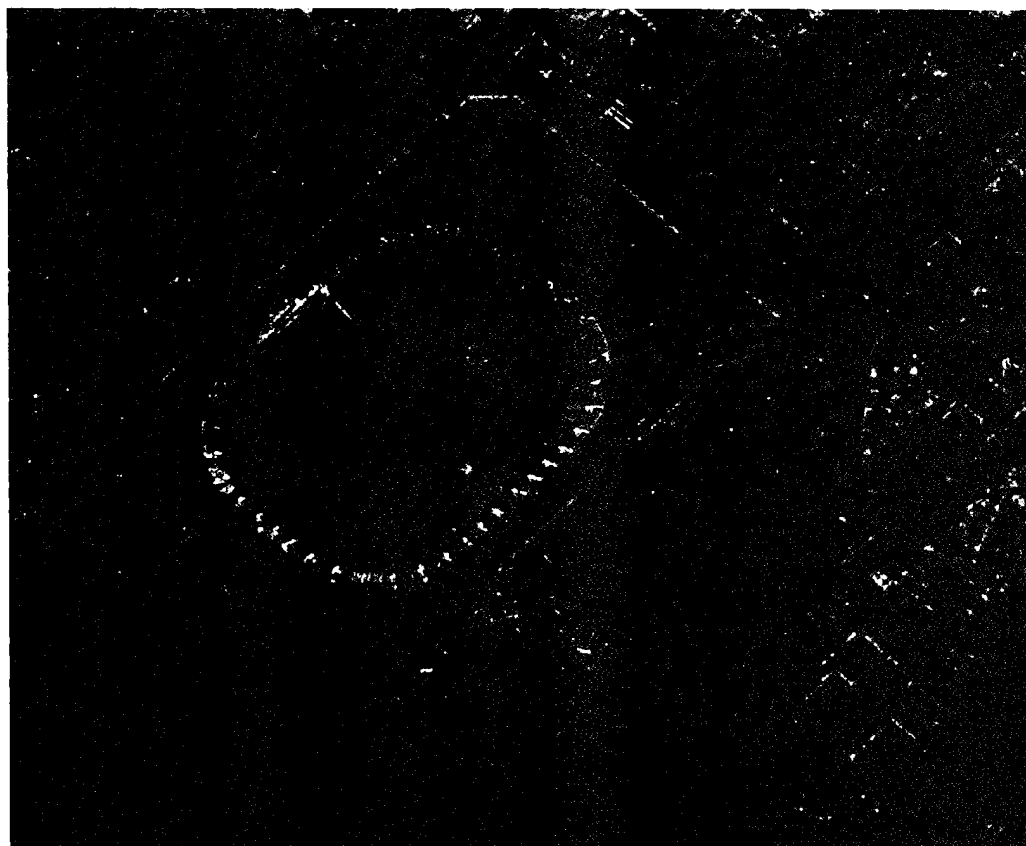


relative  
intensity

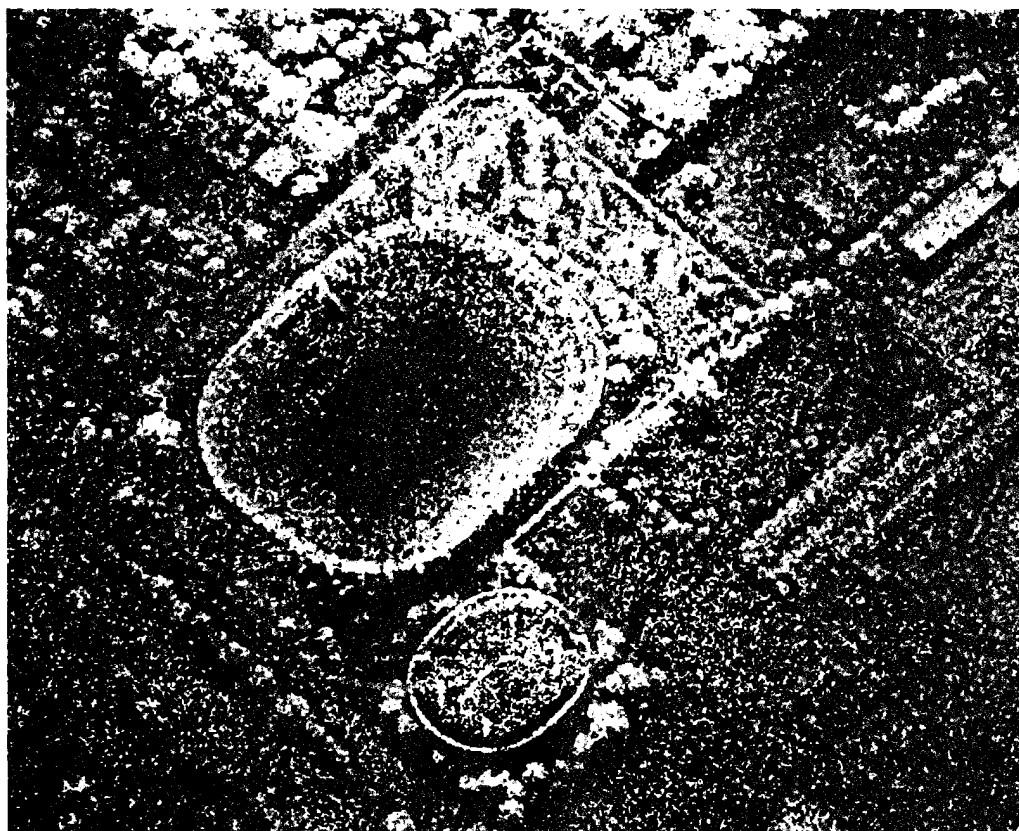


interferometric  
phase (deg)  
3X3 ideal LPF

Figure 20: SVA interferogram.



relative  
intensity



interferometric  
phase (deg)  
3X3 ideal LPF

Figure 21: ASR (order 4,  $c=.25$ ) interferogram.